Ji, M., Gao, X.Y., and Zheng, Y.F., 2023, Progressively elevated geothermal gradients for Miocene metamorphism in the Himalayan orogen: GSA Bulletin, https://doi.org/10.1130/B36892.1.

# Supplemental Material

**Supplemental Text S1.** Methods.

**Figure S1.** The location and elevation of three types of granitic gneisses from the Cona area, southern Tibet, in the eastern Himalaya.

**Figure S2.** Selected oxides versus $SiO_2$ for granitic gneisses with Neoproterozoic and Early Paleozoic protolith ages in this study and literature along the Himalayan orogen.

**Figure S3.** Whole-rock major element compositions for three types of granitic gneiss from the Cona area, southern Tibet, in the eastern Himalaya.

**Figure S4.** Chondrite normalized rare earth element (REE) patterns (a, c) and primitive mantle normalized trace element spider diagrams (b, d) for granitic gneisses with Neoproterozoic and Early Paleozoic protolith age in this study and literature along the Himalayan orogen.

**Figure S5.** Representative Raman spectra of diagnostic minerals in Type III granitic gneiss 15XZ93 from the Cona area, southern Tibet, in the eastern Himalaya.

**Figure S6.** Garnet X-ray compositional elementary (Ca, Fe, Mg, and Mn) maps for three types of granitic gneisses from the Cona area, southern Tibet, in the eastern Himalaya.

**Figure S7.** Photomicrographs and compositional profiles of another garnet porphyroblasts for three types of granitic gneisses from the Cona area, southern Tibet, in the eastern Himalaya.

**Figure S8.** Photomicrographs of three types of granitic gneisses from the Cona area, southern Tibet, in the eastern Himalaya in microscopic cathodoluminescence (a–f) and compositional profiles of plagioclase (g–i).

**Figure S9.** Diagrams of representative trace element contents and ratios for zircon from three types of granitic gneisses from the Cona area, southern Tibet, in the eastern Himalaya.

**Figure S10.** BSE images of monazite inclusions for three types of granitic gneisses from the Cona area, southern Tibet, in the eastern Himalaya.

**Figure S11.** Garnet single component diffusion modeling for Type I granitic gneiss 15XZ120 from the Cona area, southern Tibet, in the eastern Himalaya.

**Figure S12.** Garnet single component diffusion modeling for Type II granitic gneiss 15XZ88 from the Cona area, southern Tibet, in the eastern Himalaya.

**Figure S13.** Garnet single component diffusion modeling for Type III granitic gneiss 15XZ93 from the Cona area, southern Tibet, in the eastern Himalaya.

**Figure S14.** $T$–$M_{O2}$ and $T$–$M_{H2O}$ pseudosections modelled by software Perple_X 6.8.5 using XRF-based compositions for three types of granitic gneisses from the Cona area, southern Tibet, in the eastern Himalaya.

**Figure S15.** $T$–$M_{O2}$ and $T$–$M_{H2O}$ pseudosections modelled by software Perple_X 6.8.5 using point count-based compositions for Type I and II granitic gneisses from the Cona area, southern Tibet, in the eastern Himalaya.

**Figure S16.** Polynomial fitting of compositional zoning as a function of x into quadrinomial for garnet from Type I gneiss 15XZ120.

**Figure S17.** Polynomial fitting of compositional zoning as a function of x into quadrinomial for garnet from Type II gneiss 15XZ88.

**Figure S18.** Polynomial fitting of compositional zoning as a function of x into quadrinomial for garnet from Type III gneiss 15XZ93.

**Figure S19.** $T$–$X$ pseudosections modelled by software Perple_X 6.8.5 using the primary and core-removed compositions for three types of granitic gneiss from the Cona area, southern Tibet, in the eastern Himalaya.

**Figure S20.** $P$–$T$ pseudosections modelled by software Perple_X 6.8.5 using the XRF-based whole-rock compositions for Type I and II granitic gneisses from the Cona area, southern Tibet, in the eastern Himalaya.

**Figure S21.** (a) Zircon and monazite U–Th–Pb ages show characteristic trends against the elevations and the distances below the STDS for these dated granitic gneisses from north to south along the N-S transect. (b) Summary of zircon $^{206}Pb/^{238}U$ ages (in red color) and monazite $^{208}Pb/^{232}Th$ ages (in blue color) for three types of granitic gneisses from the Cona area, southern Tibet, in the eastern Himalaya.

**Figure S22.** The pie chart diagrams show the light-rare earth elements (LREE), heavy-rare earth elements (HREE), and Y contents that each mineral contained according to the whole-rock trace element mass balance calculation for important REE-bearing minerals in three types of granitic gneisses from the Cona area, southern Tibet, in the eastern Himalaya.

**Figure S23.** (a) A schematic diagram for trace element partition between garnet and zircon/monazite during garnet growth and resorption process. Chondrite normalized REE patterns of garnet (b) and the calculated partition coefficients of REE between zircon and garnet (c) and monazite and garnet (d) for Type III gneiss 15XZ93 from the Cona area, southern Tibet, in the eastern Himalaya.

**Table S1.** Locations and mineral assemblages of three types of granitic gneisses from the Cona area, southern Tibet, in the eastern Himalaya.

**Table S2.** Whole-rock major and trace element compositions for three types of granitic gneisses from the Cona area, southern Tibet, in the eastern Himalaya.

**Table S3.** Major elements of garnet for three types of granitic gneisses from the Cona area, southern Tibet, in the eastern Himalaya.

**Table S4.** Major elements of mica for three types of granitic gneisses from the Cona area, southern Tibet, in the eastern Himalaya.

**Table S5.** Major elements of feldspar for three types of granitic gneisses from the Cona area, southern Tibet, in the eastern Himalaya.

**Table S6.** Summary of mineral chemistry for three types of granitic gneisses from the Cona area, southern Tibet, in the eastern Himalaya.

**Table S7.** Representative primary data from EPMA analyses for garnet, biotite, plagioclase, and K-feldspar in three types of granitic gneisses from the Cona area, southern Tibet, in the eastern Himalaya.

**Table S8.** LA-ICPMS zircon U–Th–Pb isotopes and trace elements for three types of granitic gneisses from the Cona area, southern Tibet, in the eastern Himalaya.

**Table S9.** LA-ICPMS monazite U–Th–Pb isotopes and trace elements for three types of granitic gneisses from the Cona area, southern Tibet, in the eastern Himalaya.

**Table S10.** Summary of investigated zircon and monazite isotope ages, trace elements, and mineral inclusions for three types of granitic gneisses from the Cona area, southern Tibet, in the eastern Himalaya.

**Table S11.** U–Th–Pb isotopes and trace elements for secondary standards during the LA-ICPMS analyses.

**Table S12.** LA-ICPMS garnet trace elements for three types of granitic gneisses from the Cona area, southern Tibet, in the eastern Himalaya.

**Table S13.** Whole-rock major element compositions used in phase equilibrium modeling for three types of granitic gneisses from the Cona area, southern Tibet, in the eastern Himalaya.

**Table S14.** Representative mineral major elements used for constraining the metamorphic *P–T* conditions of three types of granitic gneisses from the Cona area, southern Tibet, in the eastern Himalaya.

**Table S15.** Comparison of observed and modelled mineral modes at the solidus for three types of granitic gneisses from the Cona area, southern Tibet, in the eastern Himalaya.

**Table S16.** Calculation of whole-rock trace element mass balance for important REE-bearing minerals in three types of granitic gneisses from the Cona area, southern Tibet, in the eastern Himalaya.

**Table S17.** Calculated partition coefficients of REE between zircon/monazite and garnet for Type III granitic gneiss from the Cona area, southern Tibet, in the eastern Himalaya.

**Table S18.** Summary of whole-rock major and trace elements for granitic gneisses with Neoproterozoic protolith age in the Himalayan orogen in literature.

**Table S19.** Summary of whole-rock major and trace elements for granitic gneisses with Early Paleozoic protolith age in the Himalayan orogen in literature.

Ji, M., Gao, X.Y., and Zheng, Y.F., 2023, Progressively elevated geothermal gradients for Miocene metamorphism in the Himalayan orogen: GSA Bulletin, https://doi.org/10.1130/B36892.1.

# Supplementary Methods

## S1.1 Sample preparation

After removing the altered and weathered surface layers, fresh hand specimens were cut into several small blocks, some for thin section production at China Geological Museum, Beijing, China, and others for whole-rock power production and mineral separation at Yuneng Rock and Mineral Separation Technology Co., Ltd., Langfang, China. As these granitic gneisses are characterized by gneissosity, two thin sections were made perpendicular and parallel to the foliation, respectively. At least 100 g of fresh blocks were crushed and then powdered in the agate grinder to ensure that the grain sizes of whole-rock powers are less than 200 mesh. Monazite and zircon were picked out roughly from the crushed sample blocks (ca. 80 mesh) in different stages using the standard magnetic and density separation technologies, and then they were handpicked carefully under the binocular microscope. Separated monazite and zircon grains were mounted in epoxy resin and polished to expose 1/3 to 1/2 of most grains at Sample Solution Analytical Technology Co., Ltd., Wuhan, China.

## S1.2 Whole-rock major and trace element

Whole-rock major elements were determined by X-ray fluorescence (XRF) using the lithium metaborate fusion method, while trace elements were analyzed by inductively coupled plasma mass spectrometry (ICPMS) using the acid dissolution method. These analyses were conducted at the ALS Chemex Laboratory, Guangzhou, China. Analytical quality is monitored by the analysis of standard materials, blank, and repeating samples within the same batch. For major elements and most trace elements, analytical uncertainties are below ±2% and ±5%, respectively. Whole-rock major and trace element compositions for these granitic gneisses are listed in Supplementary Table S2. The compositions of Chondrite and Primitive Mantle are from Sun and McDonough (1989) and McDonough and Sun (1995), respectively.

## S1.3 Petrological observation

Modern petrological techniques were applied to identify the petrographic texture of these granitic gneisses at Chinese Academy of Sciences (CAS) Laboratory of Crust-Mantle Materials and Environment in University of Science and Technology of China (USTC), Hefei, China.

Micro-X-ray fluorescence (Micro-XRF) maps were obtained using Bruker M4 TORNADO with working conditions of 50 kV and 200 μA. Mineral distribution maps of thin sections and mineral modal proportions were constructed with the software ARMICS.

Microscope cathodoluminescence (CL) was conducted with Beacon Innovation CLF-2 system. Under the operation conditions of 15 kV and 500 μA, K-feldspar is blue, plagioclase is dark green, kyanite is red, sillimanite is dark red, while garnet, biotite, muscovite, and quartz are dark.

Backscattered electron (BSE) imaging, zircon CL imaging, and identification of unknown minerals were performed using TESCAN MIRA3 SEM equipped with Mono CL system and Oxford INCA energy dispersive spectrometer (EDS). The working conditions are 15 kV and 15 nA for BSE imaging and EDS, and 10 kV and 18 nA for CL imaging.

Garnet X-ray compositional elementary (Ca, Fe, Mg, and Mn) maps were obtained using Shimadzu EPMA-1600. The working conditions were as follows: accelerating voltage of 15 kV, beam current of 50 nA, dwell time of 50 ms, beam size of 1 μm, and step size of 10 μm.

Mineral inclusions and polymorph minerals such as kyanite and sillimanite were identified by JY HORIBA LabRam HR equipped with a confocal microscope, an air-cooled CCD detector, and a 532 nm laser excitation, with a beam size of 1 μm.

## S1.4 Mineral major element

Mineral major elements were determined in thin sections using Shimadzu EPMA-1600 at USTC. The working conditions were as follows: accelerating voltage of 15 kV, beam current of 10–20 nA (10 nA for mica, 15 nA for feldspar, and 20 nA for garnet), and beam size of 1–5 μm (1 μm for mica and garnet and 5 μm for feldspar). Garnet, mica, and feldspar were also analyzed using JXA-8530F Plus at USTC with the accelerating voltage of 15 kV, the beam current of 10 nA, and the beam size of 5 μm. Natural standards were used for calibration, and ZAF correction methods were applied to the raw data. For important major elements in each mineral, the analytical errors were below ±5%. The analytical results of garnet, mica, and feldspar are listed in Supplementary Tables S3, S4, and S5, respectively. The representative primary data showing the analytical error is presented in Supplementary Table S7.

## S1.5 Mineral U–Th–Pb isotope and trace element

Zircon U–Th–Pb isotopes and trace elements were simultaneously analyzed in mounted grains at USTC using an Agilent 7900 Q-ICPMS coupled to a GeoLas-HD 193nm excimer laser ablation system. Zircon grains were ablated with a spot size of 24 or 32 μm, an energy of 60 mJ, and a repetition rate of 4 Hz. Helium was used as the carrier gas and mixed with make-up gas argon prior to introduction into the ICPMS. Each analysis includes 20 s of background acquisition and 70 s of data acquisition. Natural zircon 91500 (1065 Ma by TIMS) (Wiedenbeck et al., 1995) was used as an external standard to correct the isotope fraction, while GJ-1 (mean $^{206}Pb/^{238}U$ age of 599.8 ± 1.7 Ma by TIMS) (Jackson et al., 2004) was applied as a secondary standard to evaluate the accuracy and precision. The weighted mean $^{206}Pb/^{238}U$ age of analyzed GJ-1 is 600.4 ± 0.7 Ma (2σ; MSWD = 0.65, n = 34), which is consistent with the recommended value. All of these standard zircons were analyzed before and after five analyses on unknown samples. The raw data were processed by the software ICPMSDataCal (Liu et al., 2010). Trace element compositions of zircon were calibrated using multiple external standard glasses (NIST610, NIST612, BIR-2G, BCR-1G, and BHVO-2G) and Si as an internal standard. A secondary standard CGSG-1 was analyzed to assess accuracy and precision. The uncertainty is better than ±10% for important trace elements. Zircon U–Th–Pb isotope and trace element data are provided in Supplementary Table S8.

Monazite U–Th–Pb isotopes and trace elements were simultaneously investigated in mounted grains using an Agilent 7500a Q-ICPMS equipped with a Geolas 193nm excimer laser ablation system at State Key Laboratory of Lithospheric Evolution in Institute of Geology and Geophysics, CAS, Beijing, China. The laser sampling was performed with an energy of 85 mJ at a repetition rate of 4 Hz using a small spot size of 24 μm, and Helium was used as the carrier gas. Data acquisition in ICPMS consists of approximately 20–25 s of background and 45–50 s of sample. Matrix-matched monazite standard Delaware 44069 (mean $^{207}Pb/^{235}U$ age of 424.89 ± 0.35 Ma by TIMS) (Aleinikoff et al., 2006) was used to correct the isotope fractionation and instrumental mass discrimination. Secondary standard monazites Maine 1 (weighted mean $^{208}Pb/^{232}Th$ age of 289.2 ± 1.6 Ma by LA-ICPMS) (Liu et al., 2012), Jefferson County ($^{206}Pb/^{238}U$ age of 363.98 ± 0.74 Ma by TIMS) and Madagascar ($^{206}Pb/^{238}U$ age of 511.3 ± 4.9 Ma by TIMS) (Peterman et al., 2012) were measured to evaluate the accuracy and precision of the analyses. The obtained weighted mean Th–Pb ages of Maine 1 (286.7 ± 2.3 Ma, 2σ, MSWD = 1.7, n = 8), Jefferson (362.1 ± 2.9 Ma, 2σ, MSWD = 0.16, n = 8) and Madagascar (518.6 ± 3.3 Ma, 2σ, MSWD = 0.04, n = 8) are identical to the recommended values. All of these standard monazites were analyzed before and after seven analyses on unknown samples. The data

reduction was processed by the software GLITTER 4.4. Trace element compositions of monazite were calculated using NIST610 as an external standard, Ce as an internal standard, and NIST612 as a secondary standard. The uncertainty of analysis is better than ±10% for important trace elements. Monazite U–Th–Pb isotope and trace element data are provided in Supplementary Table S9.

U–Th–Pb isotopes of secondary standards during the LA-ICPMS analyses of zircon and monazite are listed in Supplementary Table S11. The concordant age plots of zircon and monazite were conducted using Isoplot 4.15 (Ludwig, 2008), and the decay constants of $^{238}U$, $^{235}U$, $^{232}Th$ recommended by Steiger and Jäger (1977) were applied in these plots.

Garnet trace elements were determined in thin sections at USTC using an Agilent 7900 Q-ICPMS coupled to a GeoLas-HD 193nm excimer laser ablation system. Garnet grains were ablated with a spot size of 24 μm, an energy of 100 mJ at a repetition rate of 4 Hz. Helium was used as the carrier gas and mixed with make-up gas argon prior to introduction into the ICPMS. Each analysis includes 20 s of background acquisition and 70 s of data acquisition. Multiple external standard glasses of NIST610, NIST612, BIR-2G, BCR-1G, and BHVO-2G were applied as external standards. Trace element compositions were calibrated using multiple external standards without applying an internal standard, which is processed by the software ICPMSDataCal (Liu et al., 2008, 2010). A secondary standard CGSG-1 was analyzed to assess accuracy and precision. The uncertainty is better than ±10% for important trace elements. Garnet trace element compositions are provided in Supplementary Table S12.

## S2.1 Garner single-component diffusion modeling

In order to quantitatively compare the diffusion rates of Mn, Fe, Mg, and Ca in garnet, we conduct single-component diffusion modeling using the spherical diffusion equation (Crank, 1975),

$$\frac{\partial C}{\partial t} = D\left(\frac{\partial C}{\partial r^2} + \frac{2\partial C}{r\partial r}\right) \quad (1)$$

where $C$ is the concentration of a component, $t$ is time, $r$ is radius (distance), $D$ is the diffusion coefficient. It is assumed that spherical garnet is sectioned through the center and its composition varies only in the radial direction (Shinevar et al., 2021). The used diffusion coefficients are from Chu and Ague (2015).

As revealed by phase equilibrium modeling for felsic rocks (e.g., Yakymchuk et al., 2017), garnet growth occurred during the prograde to peak stage (M1–M2), while garnet breakdown and resorption took place during the retrograde stage (M2–M3). At the peak M2 stage with the highest temperatures, the compositional profile in garnet is likely to be homogeneous, which is the general assumption in diffusion modeling of Zou et al. (2021). For example, garnet grain that do no preserve growth zoning, as is the case of garnet in Type I gneiss 15XZ120. Owing to the small grain size of 0.7 mm, compositional homogenization is possible to be achieved in the garnet core by diffusion at the peak stage. However, some garnet grains with large sizes are able to preserve growth zoning, such as the garnet in Type II gneisses 15XZ88 (1.6 mm) and 15XZ93 (2.5 mm). In these cases, diffusion at the peak stage exerts limited effects on garnet core, and compositional homogenization is only achieved at garnet rim.

For garnet grains in Type I gneiss 15XZ120 with weak zoning in the core, the compositional profile was most likely been homogenized at the peak stage (Fig. 5b). Thus, the initial condition is assumed that compositional profile of garnet (A–>B) is homogeneous whereas the composition of outmost rim (B) is different, and the boundary is assumed to be fixed during diffusion (Fig. S11). By contrast, for garnet grains in Type II 15XZ88 and Type III 15XZ93 gneisses with growth zoning in the core (Figs. 5d and 5f), the compositional

homogenization is only achieved at the rim. Thus, the initial condition is assumed that the compositional profile of garnet rim (A–>B) is homogeneous whereas the composition of outmost rim (B) is different, and the boundary is assumaed to be fixed during diffusion (Figs. S12 and S13). Garnet diffusion modeling was performed under $P$–$T$–$f_{O2}$ conditions of M2 to M3 and carbon-carbon dioxide (CCO) oxygen fugacity buffer from the garnet core or the outmost core to the outmost rim (A–>B).

The modelled results show that the diffusion rate of Mn is the fastest, the diffusion rate of Ca is the slowest, while the diffusion rates of Fe and Mg fall in between those of the Mn and Ca. In this sense, if the retrograde process lasted for 5–16 m.y. to fit the Ca zoning, the Mn, Fe, and Mg zonings are modified more extensively by diffusion in such a long time. As a consequence, $X_{Grs}$ in the garnet core is most likely to preserve the composition of the prograde to peak stage.

## S2.2 Phase equilibrium modeling

Phase equilibrium modeling were performed in the system MnNCKFMASHTO, using Perple_X 6.8.5 (Connolly, 2005; Connolly and Galvez, 2018) with an internally consistent thermodynamic dataset of hp62ver.dat (Holland and Powell, 2011) and fluid equation of state of Holland and Powell (1998). The used solid solution models include silicate melt, garnet, muscovite, biotite, orthopyroxene, cordierite (White et al., 2014), plagioclase and K-feldspar (Holland and Powell, 2003), clinopyroxene (Holland and Powell, 1998), spinel (White et al., 2002), and ilmenite (White et al., 2000). Kyanite, sillimanite, rutile, quartz, and $H_2O$ were considered as pure phases.

Three representative granitic gneisses that have been conducted detailed petrological observations were selected for phase equilibrium modeling. At first, the XRF-based whole-rock compositions were used in the calculation, $P_2O_5$, CaO, $H_2O$, and $O_2$ ($Fe_2O_3$) need special treatment. Given that whole-rock $P_2O_5$ contents are only enriched in accessory mineral apatite and monazite, $P_2O_5$ was deducted from whole-rock major elements and the content of CaO was corrected at the same time. The amounts of $H_2O$ and $O_2$ ($Fe_2O_3$) were determined using $T$–$M_{H2O}$ and $T$–$M_{O2}$ diagrams (Figs. S14 and S15), respectively, to ensure that final mineral assemblages are stable just above the solidus (Korhonen et al., 2013). In addition, the estimated $H_2O$ and $O_2$ ($Fe_2O_3$) contents were also verified by the modal proportion of hydrated minerals in thin sections and by $Fe^{3+}$ contents calculated based on the charge balance for major minerals, respectively.

However, the predicted mineral modes for Type I gneiss 15XZ120 and Type II gneiss 15XZ88 cannot be compared with the observed ones in the thin section. In this situation, the whole-rock compositions were recalculated by combining the mineral modes from the estimate of micro-XRF maps with mineral chemistry obtained by EPMA. The weighted average compositions were applied for zoned minerals such as garnet and plagioclase. The proportions and compositions of the garnet core were not included in the calculation. In these samples, two hydrous phases of biotite and muscovite mainly control the $H_2O$ contents in the whole-rock composition. The $H_2O$ content of biotite is calculated according to the Ti-H substitution scheme of White et al. (2007), whereas that of muscovite is calculated by stoichiometry. The amount of $O_2$ ($Fe_2O_3$) was determined similar to that of the XRF-based composition. All types of whole-rock compositions used in the phase equilibrium modeling are listed in Supplementary Table S13.

Since the garnet has pronounced compositional zoning, the effective whole-rock composition was determined by subtracting the garnet core from the measured whole-rock compositions. The strategy of subtracting the garnet core follow the method of Evans (2004) and Du et al. (2014). All garnet is assumed to be nearly spherical and have a similar compositional profile, and most of the whole-rock MnO is incorporated into the garnet. The

compositions of fractionated garnet cores were polynomial fitted as a function of x as quadrinomials (Figs. S16, S17, and S18). Therefore, the contents of major elements in garnet can be described by the following equation:

$$C_i^{\mathrm{F}}(r) = \int_0^{\mathrm{r}} 4\pi x^2 c_i(x) dx \quad (2)$$

where $C_i^{\mathrm{F}}(r)$ is the content of major element $i$ (FeO, MgO, CaO, and MnO) in the fractionated garnet core with the radius $r$, and $c_i(x)$ is the content of major element $i$ at point $x$, which can be calculated from the fitting quadrinomials of garnet zoning.

The MnO contents of the garnet core that fractionated from the whole-rock composition ($C_{\mathrm{MnO}}^{\mathrm{F}}$) can be described by the following equation:

$$C_{\mathrm{MnO}}^{\mathrm{F}} = (C_{\mathrm{MnO}}^{\mathrm{W}} - C_{\mathrm{MnO}}^{\mathrm{M}}) \frac{C_{\mathrm{MnO}}^{\mathrm{F}}(r)}{C_{\mathrm{MnO}}^{\mathrm{F}}(R)} \quad (3)$$

where $C_{\mathrm{MnO}}^{\mathrm{W}}$ and $C_{\mathrm{MnO}}^{\mathrm{M}}$ represent the MnO contents in the whole-rock composition and the matrix (here is equal to zero, as most of MnO is incorporated into the garnet), respectively.

Therefore, the contents of FeO, MgO, and CaO in the fractionated garnet core ($C_i^{\mathrm{F}}$) can be written as:

$$C_i^{\mathrm{F}} = C_{\mathrm{MnO}}^{\mathrm{F}} \frac{C_i^{\mathrm{F}}(r)}{C_{\mathrm{MnO}}^{\mathrm{F}}(r)} = C_{\mathrm{MnO}}^{\mathrm{W}} \frac{C_i^{\mathrm{F}}(r)}{C_{\mathrm{MnO}}^{\mathrm{F}}(R)} \quad (4)$$

Apart from that, garnet also contains $SiO_2$ and $Al_2O_3$, the contents of which can be described as the following equation according to the chemical formula:

$$C_{\mathrm{SiO2}}^{\mathrm{F}} = \sum_{\mathrm{i=FeO,\ MgO,\ CaO,\ MnO}} C_i^{\mathrm{F}} \quad (5)$$

$$C_{\mathrm{Al2O3}}^{\mathrm{F}} = \frac{1}{3} \sum_{\mathrm{i=FeO,\ MgO,\ CaO,\ MnO}} C_i^{\mathrm{F}} \quad (6)$$

In summary, the contents of major elements (FeO, MgO, CaO, MnO, $SiO_2$, and $Al_2O_3$) for the fractionated garnet cores can thus be deducted from the XRF-measured whole-rock composition, and get the effective whole-rock composition.

Because plagioclase grains in Type I gneiss have relatively wide compositional ranges and preserve obvious relict cores. By contrast, plagioclase grains in Type II and Type III gneisses are relatively homogeneous. As a consequence, we only investigated the influence of subtracting plagioclase core from the whole-rock composition for Type I gneiss 15XZ120. Plagioclase is assumed to have a cuboid shape, and the plagioclase cores occupies the volume fraction of 46.4 vol.%, which is estimated from the petrographic observation.

The *T–X* pseudosections modelled using primary and core-removed compositions for three types of granitic gneiss are illustrated in Fig. S19. The location where $X = 0$ represents the primary XRF-based composition, while the location where $X = 1$ represents the effective whole-rock composition from which the garnet core (Figs. S19a, S19b, and S19c) or plagioclase core (Fig. S19d) is removed. The modelled results show that whether the garnet/plagioclase core is subtracted or not has a slight effect on the topologies and mineral chemistry of the *P–T* pseudosection for these samples.

## REFERENCES

Aleinikoff, J. N., Schenck, W. S., Plank, M. O., Srogi, L., Fanning, C. M., Kamo, S. L., and Bosbyshell, H., 2006, Deciphering igneous and metamorphic events in high-grade rocks of the Wilmington Complex, Delaware: Morphology, cathodoluminescence and backscattered electron zoning, and SHRIMP U–Pb geochronology of zircon and monazite: Geological Society of America Bulletin, v. 118, no. 1-2, p. 39–64. https://doi.org/10.1130/B25659.

Chu, X., and Ague, J. J., 2015, Analysis of experimental data on divalent cation diffusion kinetics in aluminosilicate garnets with application to timescales of peak Barrovian metamorphism, Scotland: Contributions to Mineralogy and Petrology, v. 170, no. 2, p. 25. https://doi.org/10.1007/s00410-015-1175-y.

Connolly, J. A. D., 2005, Computation of phase equilibria by linear programming: a tool for geodynamic modeling and its application to subduction zone decarbonation: Earth and Planetary Science Letters, v. 236, no. 1-2, p. 524–541. https://doi.org/10.1016/j.epsl.2005.04.033.

Connolly, J. A. D., and Galvez, M. E., 2018, Electrolytic fluid speciation by Gibbs energy minimization and implications for subduction zone mass transfer: Earth and Planetary Science Letters, v. 501, p. 90–102. https://doi.org/10.1016/j.epsl.2018.08.024.

Crank, J., 1975, The mathematics of diffusion: Oxford university press. 1–414 p.

Du, J. X., Zhang, L. F., Bader, T., Chen, Z. Y., and Lü, Z., 2014, Metamorphic evolution of relict lawsonite-bearing eclogites from the (U) HP metamorphic belt in the Chinese southwestern Tianshan: Journal of Metamorphic Geology, v. 32, no. 6, p. 575–598. https://doi.org/10.1111/jmg.12080.

Holland, T., and Powell, R., 1996, Thermodynamics of order-disorder in minerals: II. Symmetric formalism applied to solid solutions: American Mineralogist, v. 81, no. 11-12, p. 1425–1437. https://doi.org/10.2138/am-1996-11-1215.

Holland, T. J. B., and Powell, R., 1998, An internally consistent thermodynamic data set for phases of petrological interest: Journal of Metamorphic Geology, v. 16, no. 3, p. 309–343. https://doi.org/10.1111/j.1525-1314.1998.00140.x.

Holland, T. J. B., and Powell, R., 2003, Activity–composition relations for phases in petrological calculations: an asymmetric multicomponent formulation: Contributions to Mineralogy and Petrology, v. 145, no.4, p. 492–501. https://doi.org/ 10.1007/s00410-003-0464-z.

Holland, T. J. B., and Powell, R., 2011, An improved and extended internally consistent thermodynamic dataset for phases of petrological interest, involving a new equation of state for solids: Journal of Metamorphic Geology, v. 29, no. 3, p. 333–383. https://doi.org/10.1111/j.1525-1314.2010.00923.x.

Jackson, S. E., Pearson, N. J., Griffin, W. L., and Belousova, E. A., 2004, The application of laser ablation-inductively coupled plasma-mass spectrometry to in situ U–Pb zircon geochronology: Chemical Geology, v. 211, no. 1-2, p. 47–69. https://doi.org/10.1016/j.chemgeo.2004.06.017.

Korhonen, F. J., Brown, M., Clark, C., and Bhattacharya, S., 2013, Osumilite–melt interactions in ultrahigh temperature granulites: phase equilibria modelling and implications for the P–T–t evolution of the Eastern Ghats Province, India: Journal of Metamorphic Geology, v. 31, no. 8, p. 881–907. https://doi.org/10.1111/jmg.12049.

Liu, Y. S., Hu, Z. C., Gao, S., Günther, D., Xu, J., Gao, C. G., and Chen, H. H., 2008, In situ analysis of major and trace elements of anhydrous minerals by LA-ICP-MS without applying an internal standard: Chemical Geology, v. 257. No. 1-2, p. 34–43. https://doi.org/10.1016/j.chemgeo.2008.08.004.

Liu, Y. S., Hu, Z. C., Zong, K. Q., Gao, C. G., Gao, S., Xu, J., and Chen, H. H., 2010, Reappraisement and refinement of zircon U-Pb isotope and trace element analyses by

LA-ICP-MS: Chinese Science Bulletin, v. 55, no. 15, p. 1535–1546. https://doi.org/10.1007/s11434-010-3052-4.

Liu, Z. C., Wu, F. Y., Yang, Y. H., Yang, J. H., and Wilde, S. A., 2012, Neodymium isotopic compositions of the standard monazites used in U–Th–Pb geochronology: Chemical Geology, v. 334, p. 221–239. https://doi.org/10.1016/j.chemgeo.2012.09.034.

Ludwig, K. R., 2008, User Manual for Isoplot/Ex Version 3.70. A geochronological toolkit for Microsoft Excel: Berkeley Geochronology Center Special Publication, no.2, p. 1–76.

McDonough, W. F., and Sun, S. S., 1995, The composition of the Earth: Chemical Geology, v. 120, p. 223–253. https://doi.org/10.1016/0009-2541(94)00140-4.

Peterman, E. M., Mattinson, J. M., and Hacker, B. R., 2012, Multi-step TIMS and CA-TIMS monazite U–Pb geochronology: Chemical Geology, v. 312, p. 58–73. https://doi.org/10.1016/j.chemgeo.2012.04.006.

Shinevar, W. J., Jagoutz, O., and VanTongeren, J. A., 2021, Gore Mountain Garnet Amphibolite Records UHT Conditions: Implications for the Rheology of the Lower Continental Crust during Orogenesis: Journal of Petrology, v. 62, no. 4, p. 1–28. https://doi.org/10.1093/petrology/egab007.

Steiger, R. H., and Jäger, E., 1977, Subcommission on geochronology: convention on the use of decay constants in geo-and cosmochronology: Earth and Planetary Science Letters, v. 36, no. 3, p. 359–362. https://doi.org/10.1016/0012-821X(77)90060-7.

Sun, S. S., and McDonough, W. F., 1989, Chemical and isotopic systematics of oceanic basalts: implications for mantle composition and processes: Geological Society Special Publications, v. 42, no. 1, p. 313–345. https://doi.org/10.1144/GSL.SP.1989.042.01.1.

White, R. W., Powell, R., Holland, T. J. B., and Worley, B. A., 2000, The effect of $TiO_2$ and $Fe_2O_3$ on metapelitic assemblages at greenschist and amphibolite facies conditions: mineral equilibria calculations in the system $K_2O$–FeO–MgO–$Al_2O_3$–$SiO_2$–$H_2O$–$TiO_2$–$Fe_2O_3$: Journal of Metamorphic Geology, v. 18, no.5, p. 497–511. https://doi.org/10.1046/j.1525-1314.2000.00269.x.

White, R. W., Powell, R., and Clarke, G. L., 2002, The interpretation of reaction textures in Fe-rich metapelitic granulites of the Musgrave Block, central Australia: constraints from mineral equilibria calculations in the system $K_2O$–FeO–MgO–$Al_2O_3$–$SiO_2$–$H_2O$–$TiO_2$–$Fe_2O_3$: Journal of Metamorphic Geology, v. 20, no. 1, p. 41–55. https://doi.org/10.1046/j.0263-4929.2001.00349.x.

White, R. W., Powell, R., and Holland, T. J. B., 2007, Progress relating to calculation of partial melting equilibria for metapelites: Journal of Metamorphic Geology, v. 25, no. 5, p. 511–527. https://doi.org/10.1111/j.1525-1314.2007.00711.x.

White, R. W., Powell, R., Holland, T. J. B., Johnson, T. E., and Green, E. C. R., 2014, New mineral activity–composition relations for thermodynamic calculations in metapelitic systems: Journal of Metamorphic Geology, v. 32, no. 3, p. 261–286. https://doi.org/10.1111/jmg.12071.

Wiedenbeck, M. A. P. C., Alle, P., Corfu, F., Griffin, W. L., Meier, M., Oberli, F., Quadt, A. V., Roddick, J. C., and Spiegel, W., 1995, Three natural zircon standards for U–Th–Pb, Lu–Hf, trace element and REE analyses: Geostandards Newsletter, v. 19, no. 1, p. 1–23. https://doi.org/ 10.1111/j.1751-908X.1995.tb00147.x.

Yakymchuk, C., Clark, C., and White, R. W., 2017, Phase relations, reaction sequences and petrochronology: Reviews in Mineralogy and Geochemistry, v. 83, no. 1, p. 13–53. https://doi.org/10.2138/rmg.2017.83.2.

Zou, Y., Li, Q., Chu, X., Zhai, M., Mitchell, R. N., Zhao, L., Zhou, L., Wang, Y., and Liu, B., 2021, Older orogens cooled slower: new constraints on Orosirian tectonics from garnet diffusion modeling of metamorphic timescales, Jiaobei terrain, North China Craton: Contributions to Mineralogy and Petrology, v. 176, no. 11, p. 91. https://doi.org/

10.1007/s00410-021-01846-w.

Ji, M., Gao, X.Y., and Zheng, Y.F., 2023, Progressively elevated geothermal gradients for Miocene metamorphism in the Himalayan orogen: GSA Bulletin, https://doi.org/10.1130/B36892.1.

# Supplementary Figures

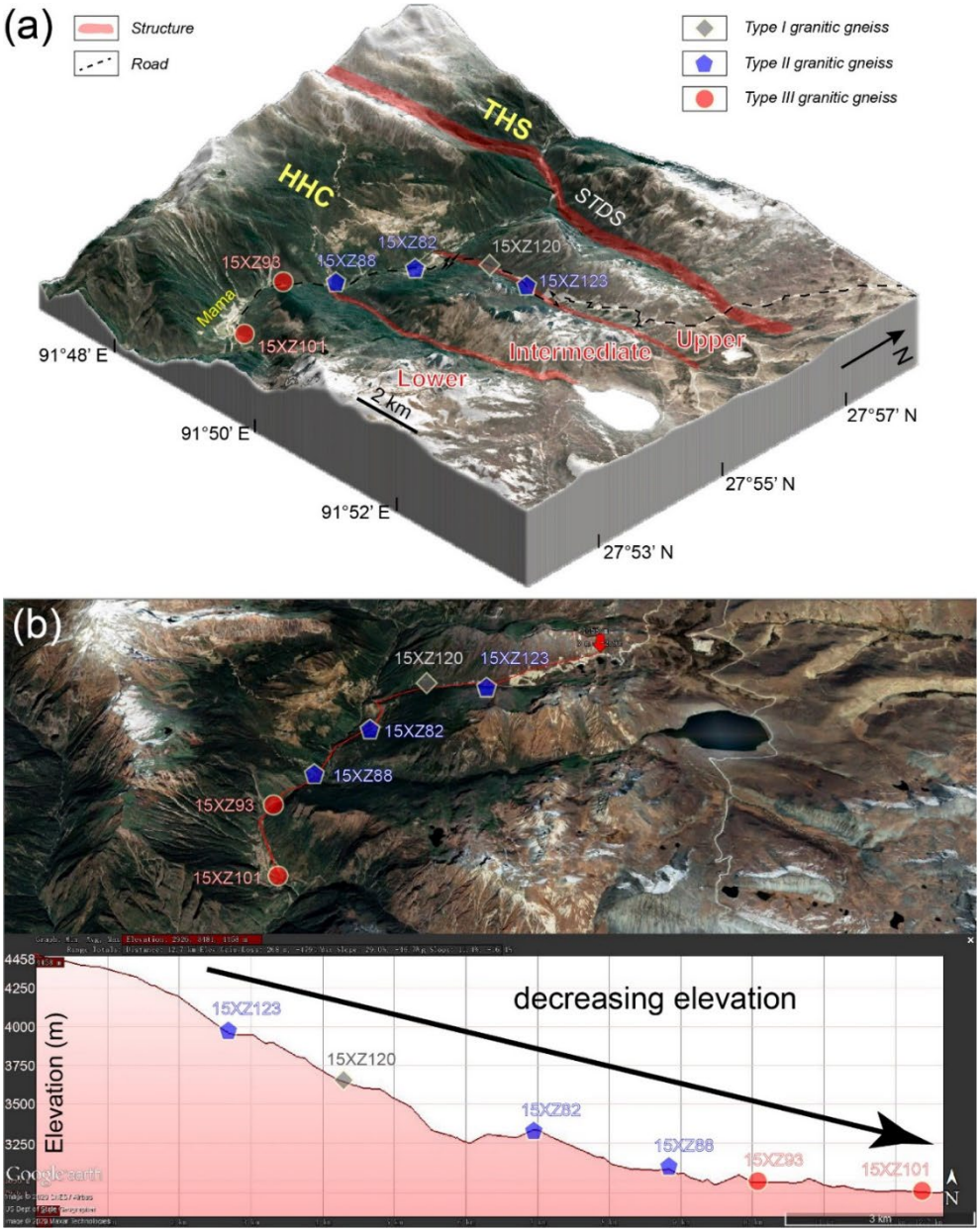


**Figure S1.** The location and elevation of three types of granitic gneisses from the Cona area, southern Tibet, in the eastern Himalaya, as is illustrated in the three-dimensional satellite map and google satellite map, respectively. (a) Three-dimensional satellite map of the Cona area shows the major lithotectonic units and structures, which was compiled from the Google map satellite imagery and the corresponding height mapper by 3D Map Generator, a PS add-in software. (b) Google satellite map of the Cona area compiled in the software Google Earth, showing the location and elevation of three types of granitic gneisses.

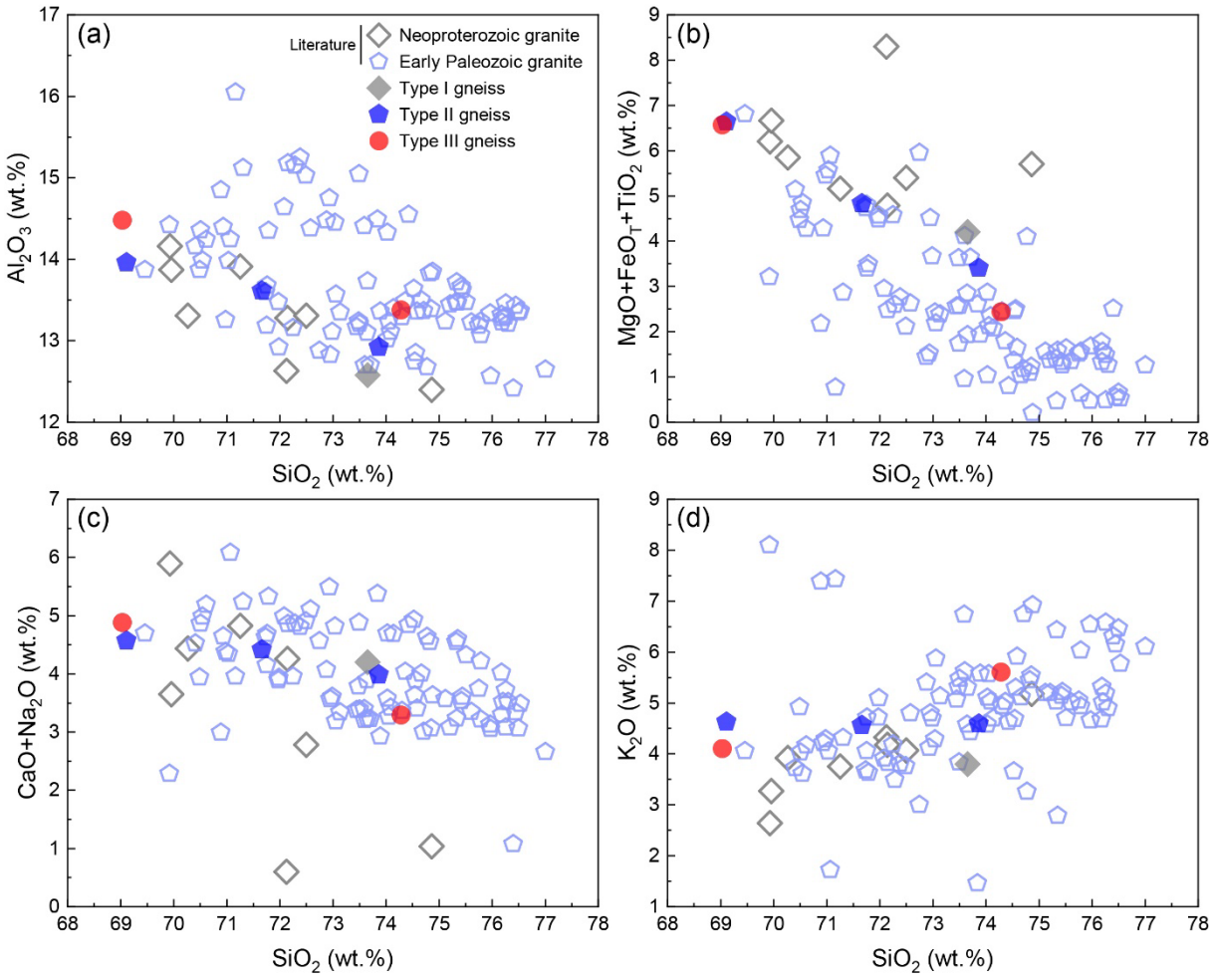


**Figure S2.** Selected oxides versus $SiO_2$ for granitic gneisses with Neoproterozoic and Early Paleozoic protolith ages in this study and literature (Wang et al., 2012, 2017a; Ding and Zhang, 2016; Gao et al., 2019) along the Himalayan orogen.

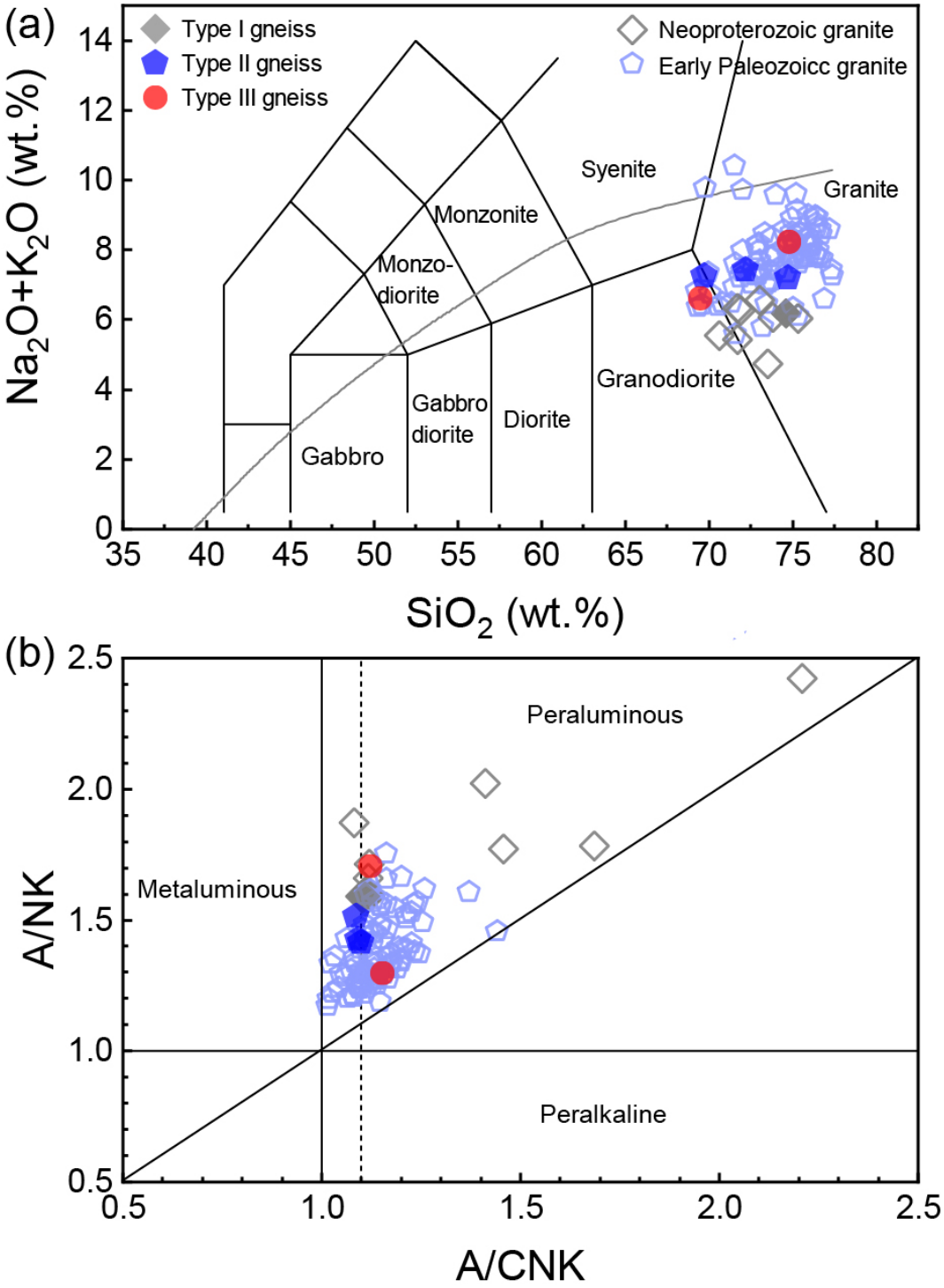


**Figure S3.** Whole-rock major element compositions for three types of granitic gneiss from the Cona area, southern Tibet, in the eastern Himalaya. Also shown are the other granitic gneisses with Neoproterozoic and Early Paleozoic protolith ages in the Himalayan orogen in literature (Wang et al., 2012, 2017a; Ding and Zhang, 2016; Gao et al., 2019). (a) Total alkali-silica classification diagrams of $Na_2O + K_2O$ versus $SiO_2$ contents. (b) A/NK versus A/CNK, where A/NK = $Al_2O_3/(Na_2O + K_2O)$ molar ratios and A/CNK = $Al_2O_3/(CaO + Na_2O + K_2O)$ molar ratios.

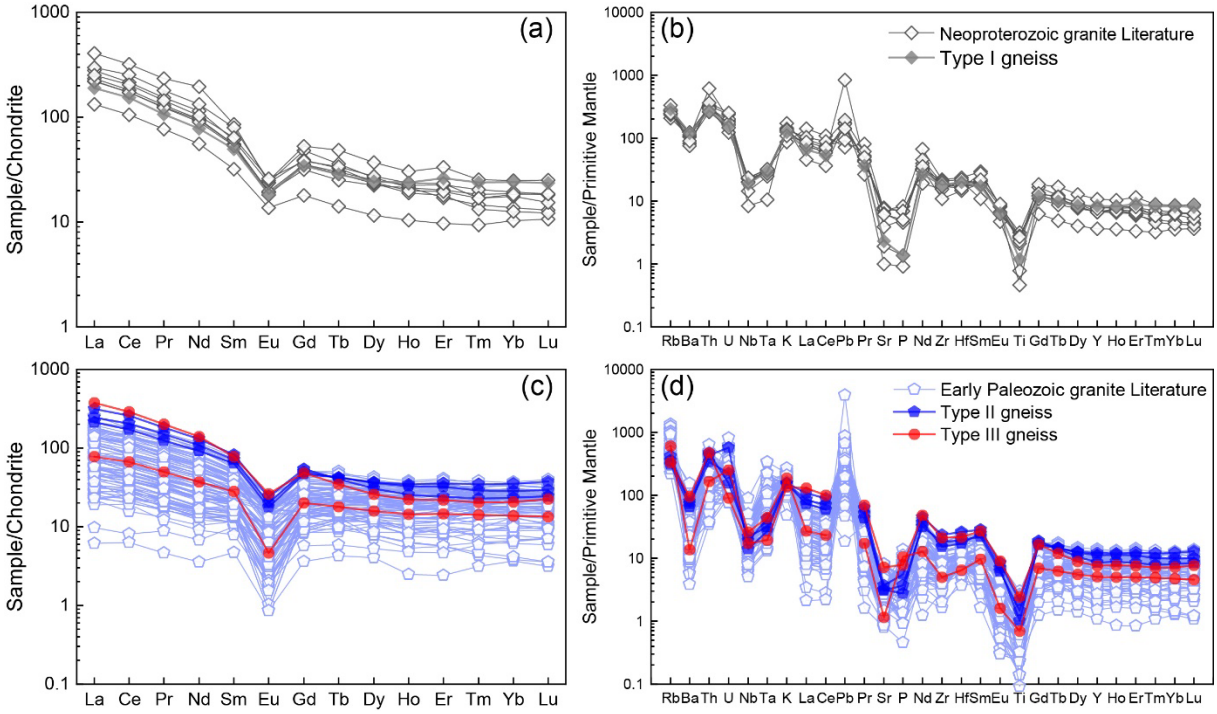


**Figure S4.** Chondrite normalized rare earth element (REE) patterns (a, c) and primitive mantle normalized trace element spider diagrams (b, d) for granitic gneisses with Neoproterozoic and Early Paleozoic protolith age in this study and literature (Wang et al., 2012, 2017a; Ding and Zhang, 2016; Gao et al., 2019) along the Himalayan orogen. The chondrite values are after Sun and McDonough (1989), and the primitive mantle values are after McDonough and Sun (1995).

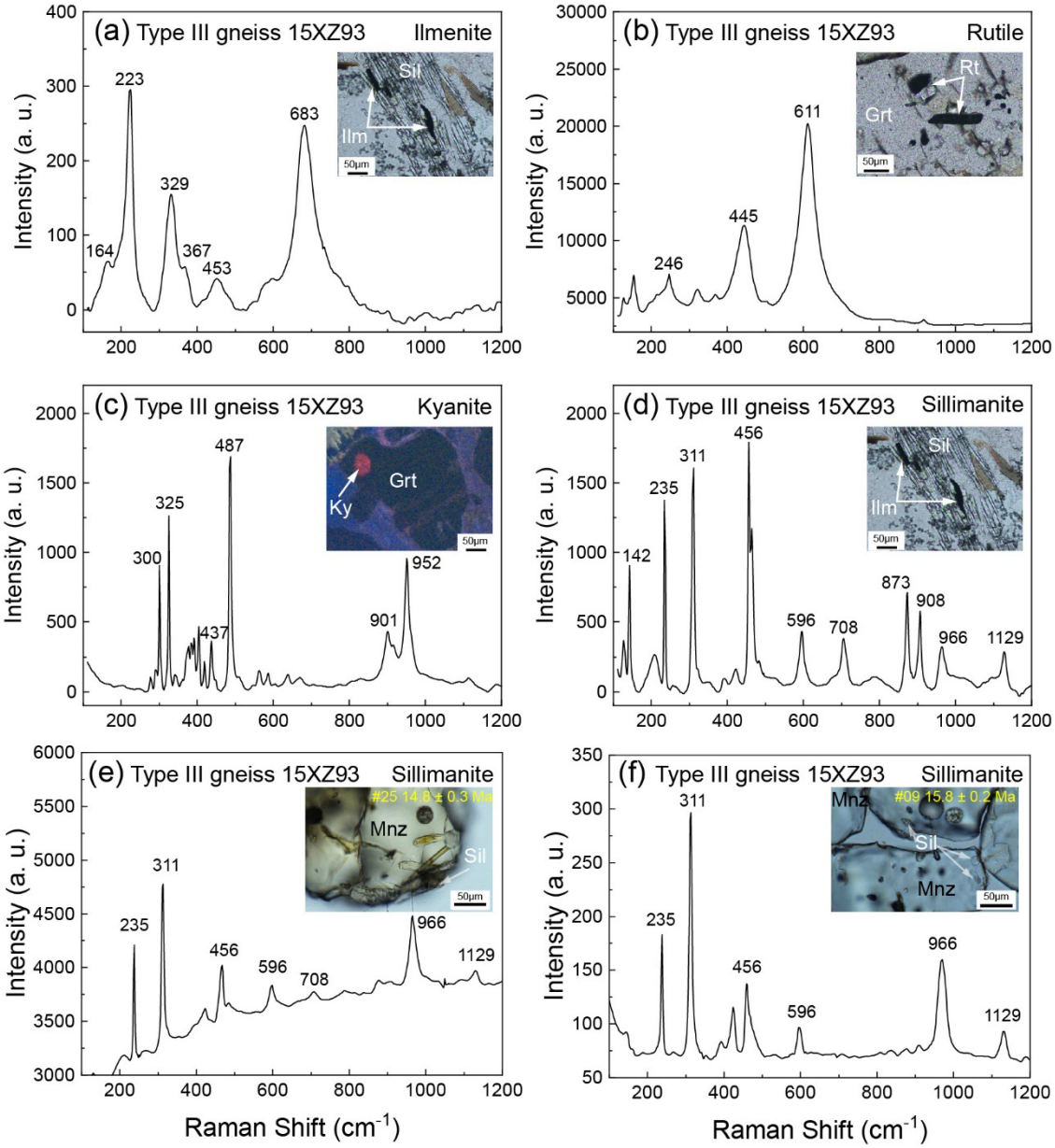


**Figure S5.** Representative Raman spectra of diagnostic minerals in Type III granitic gneiss 15XZ93 from the Cona area, southern Tibet, in the eastern Himalaya. (a) Intergrowth of ilmenite with sillimanite in the matrix. (b) Rutile inclusion in garnet. (c) Kyanite inclusion in garnet. (d) Fibrous sillimanite in the matrix. (e) Sillimanite inclusion in the monazite rim, where LA-ICPMS analysis gives Th–Pb age of 14.8 ± 0.3 Ma. (f) Sillimanite inclusion in the monazite rim, where LA-ICPMS analysis gives Th–Pb age of 15.8 ± 0.2 Ma.

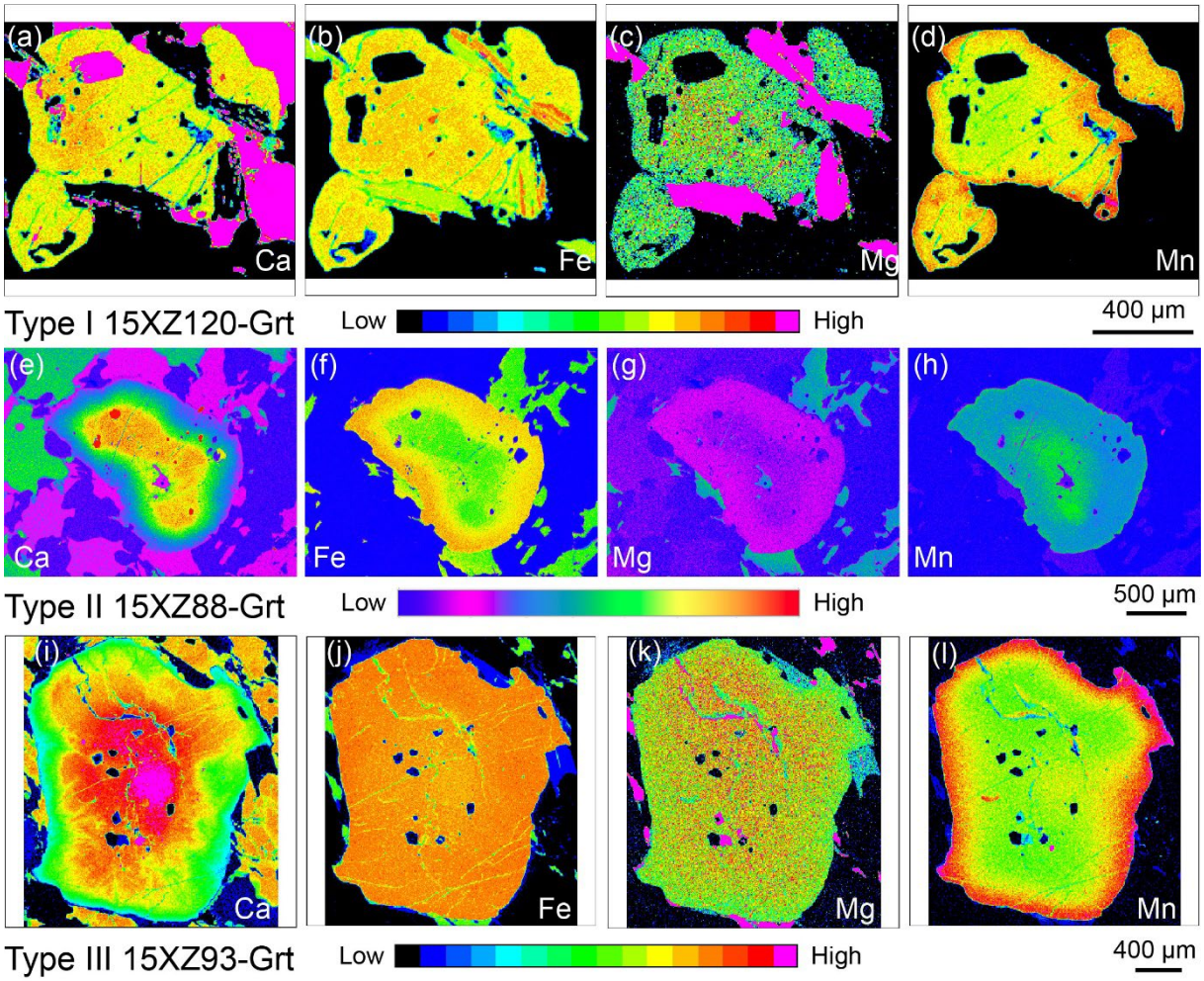


**Figure S6.** Garnet X-ray compositional elementary (Ca, Fe, Mg, and Mn) maps for three types of granitic gneisses from the Cona area, southern Tibet, in the eastern Himalaya. (a–d) Type I granitic gneiss 15XZ120. (e–h) Type II granitic gneiss 15XZ88. (i–l) Type III granitic gneiss 15XZ93.

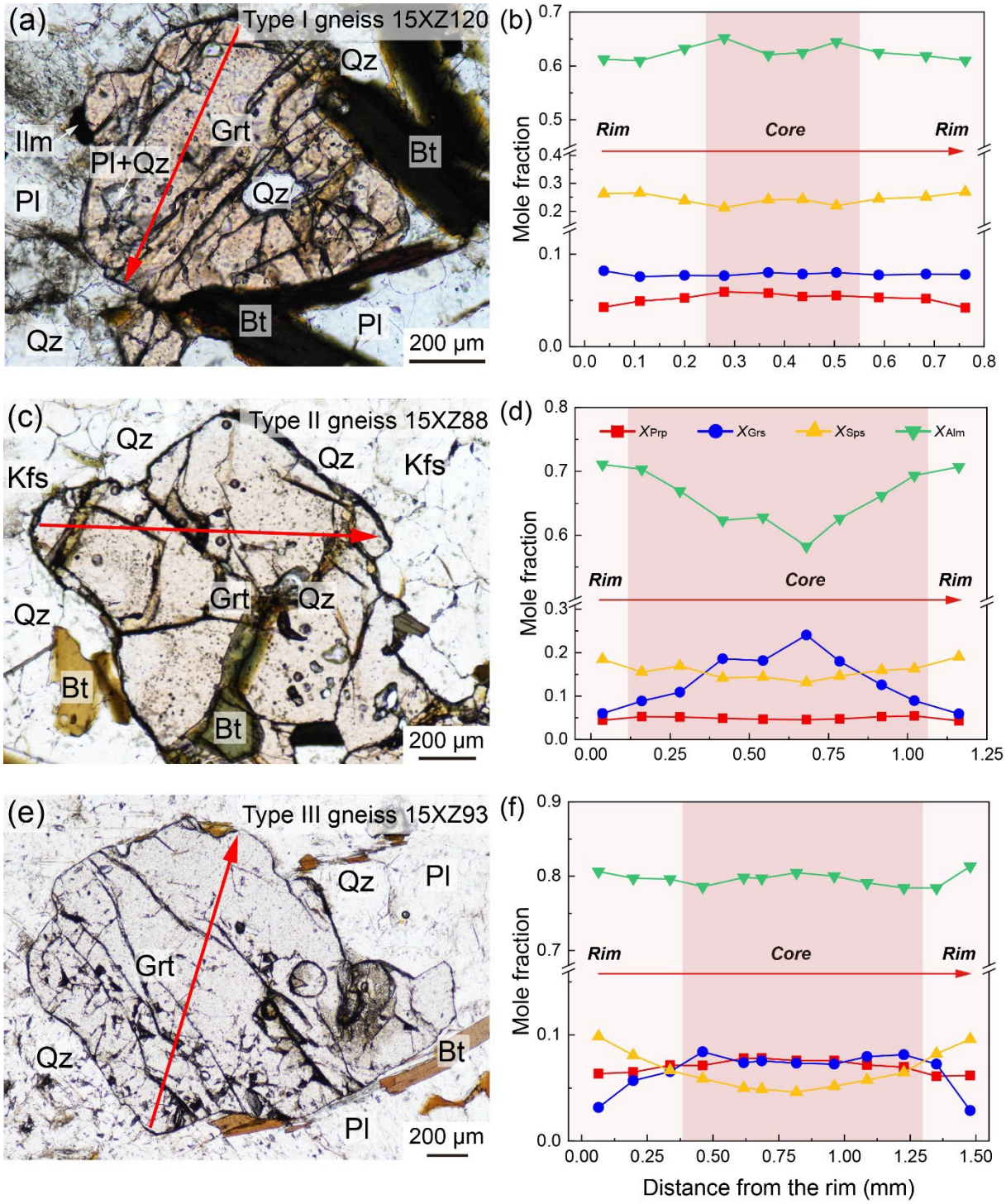


**Figure S7.** Photomicrographs and compositional profiles of another garnet porphyroblasts for three types of granitic gneisses from the Cona area, southern Tibet, in the eastern Himalaya. (a, b) Type I granitic gneiss 15XZ120. (c, d) Type II granitic gneiss 15XZ88. (e, f) Type III granitic gneiss 15XZ93.

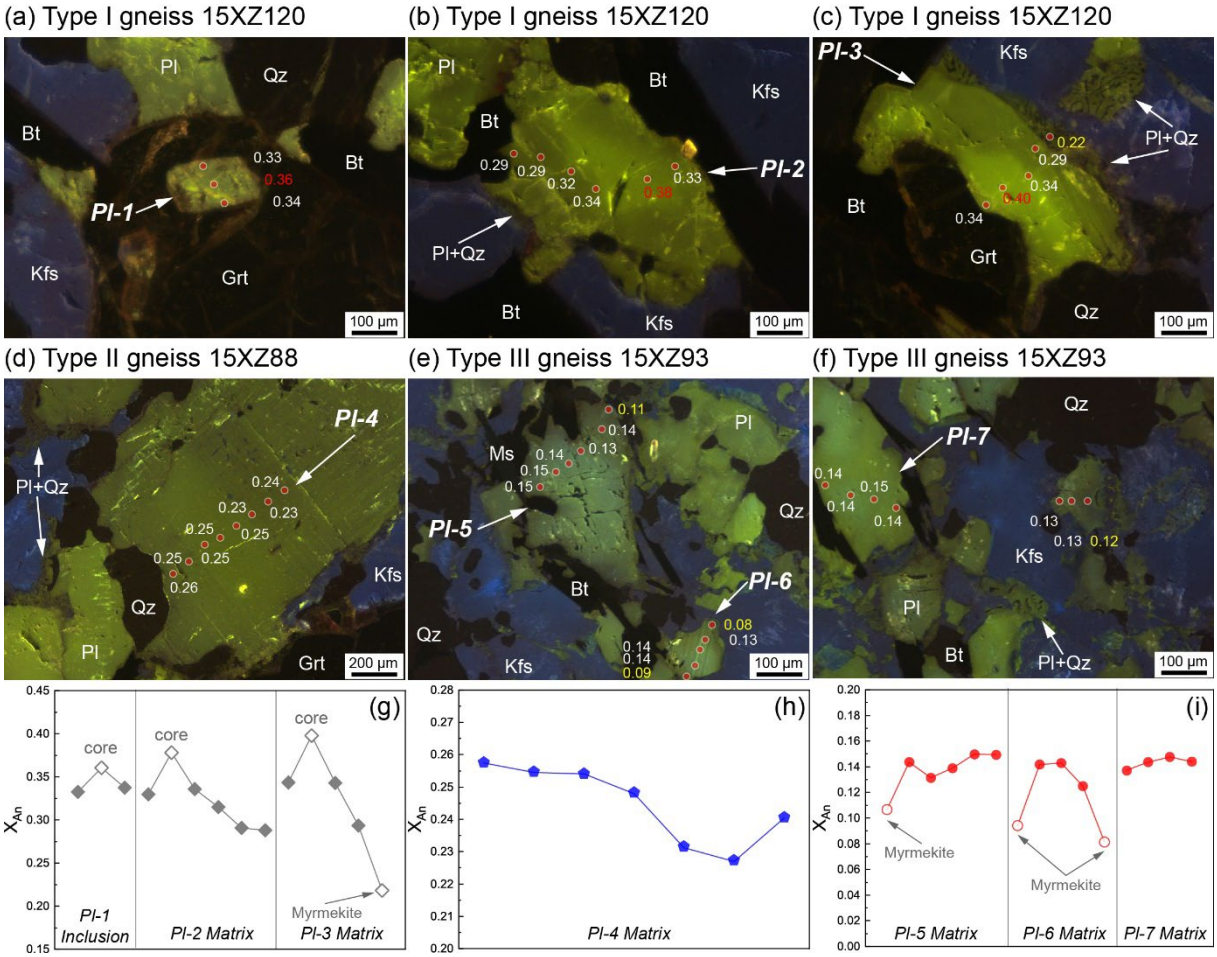


**Figure S8.** Photomicrographs of three types of granitic gneisses from the Cona area, southern Tibet, in the eastern Himalaya in microscopic cathodoluminescence (a–f) and compositional profiles of plagioclase (g–i). (a) Type I granitic gneiss 15XZ120, plagioclase inclusion (yellow) in garnet porphyroblasts (black). (b, c) Type I granitic gneiss 15XZ120, matrix plagioclase either in contact with garnet or not is zoned and characterized by bright yellow core and dark yellow rim. The plagioclase outmost rim in contact with K-feldspar is marked by the intergrowth of plagioclase and quartz representing the myrmekite. (d) Type II granitic gneiss 15XZ88, matrix plagioclase shows remarkable zoning, the outmost rim of which is dominated by the growth of myrmekite. (e, f) Type III granitic gneiss 15XZ93, the dark yellow rim overgrowths on the bright yellow core, the intergrowth of plagioclase and quartz span the plagioclase and K-feldspar. The red dots denote the analyzed points, and the number corresponds to the $X_{An}$.

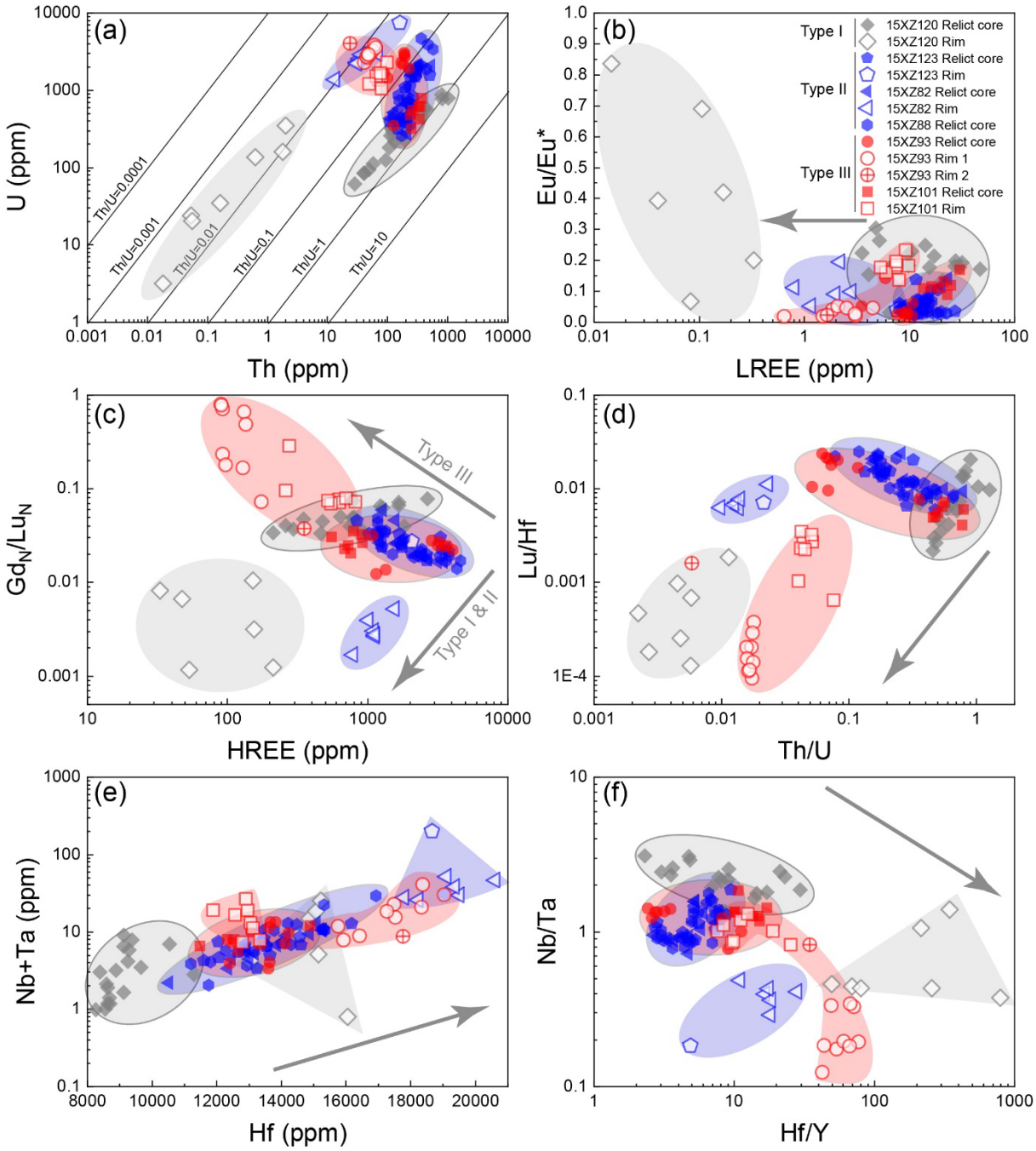


**Figure S9.** Diagrams of representative trace element contents and ratios for zircon from three types of granitic gneisses from the Cona area, southern Tibet, in the eastern Himalaya.

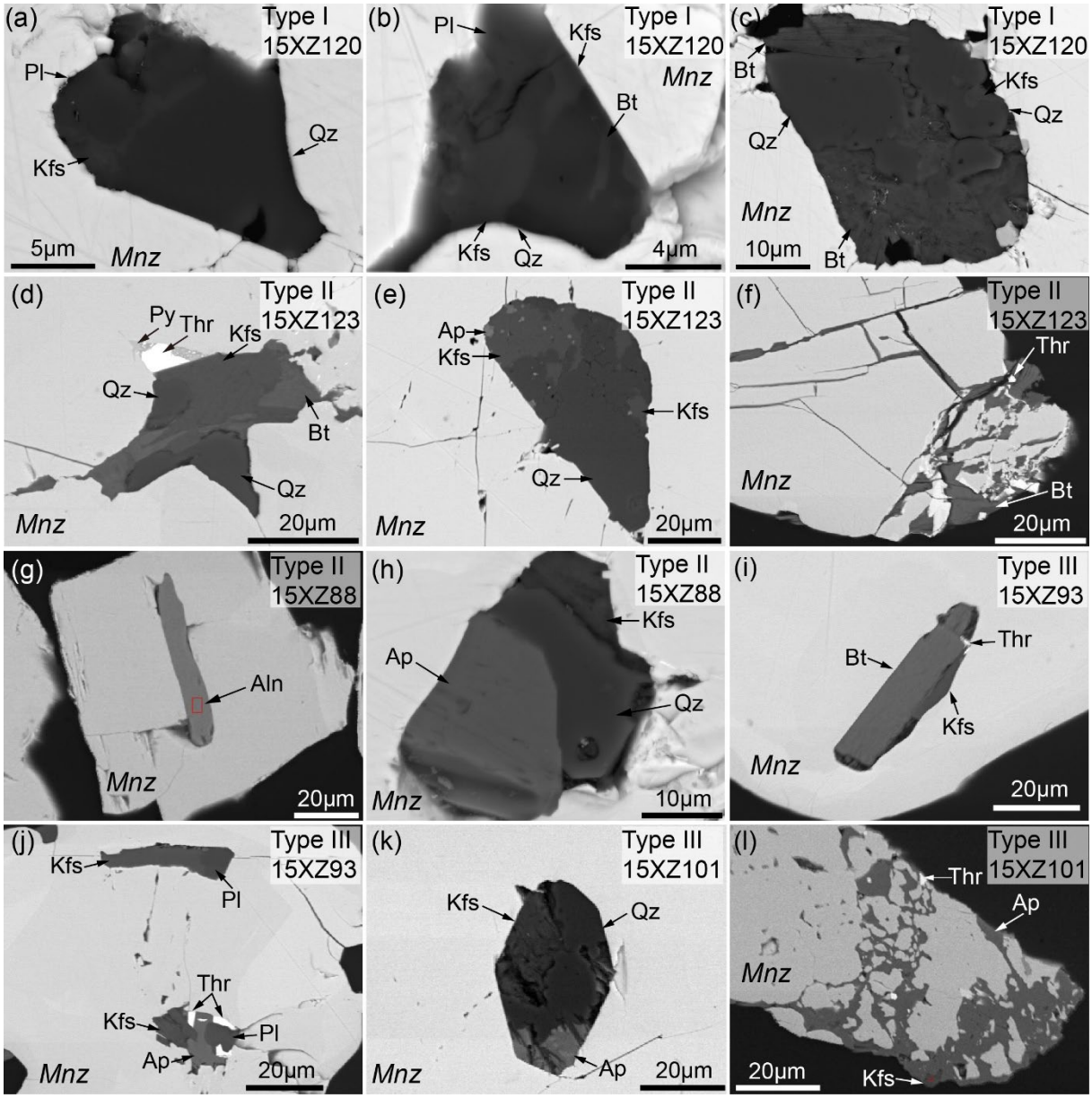


**Figure S10.** BSE images of monazite inclusions for three types of granitic gneisses from the Cona area, southern Tibet, in the eastern Himalaya. (a–c) Type I gneiss 15XZ120, multiphase crystal inclusions composed of biotite + K-feldspar + quartz + plagioclase in monazite. (d–e) Type II gneiss 15XZ123, multiphase crystal inclusions composed of biotite + K-feldspar + quartz + thorite + pyrite + apatite in monazite. (f) Type II gneiss 15XZ123, the rim of monazite is partially replaced by biotite and thorite. (g) Type II gneiss 15XZ88, allanite is included in monazite. (h) Type II granitic gneiss 15XZ88, multiphase crystal inclusion consists of K-feldspar + quartz + apatite in monazite. (i) Type III gneiss 15XZ93, monazite contains multiphase crystal inclusion is composed of biotite + K-feldspar + thorite. (j) Type III granitic gneiss 15XZ93, multiphase crystal inclusions consist of cuspate K-feldspar + plagioclase and plagioclase + K-feldspar + apatite + thorite in monazite. (k) Type III gneiss 15XZ101, multiphase crystal inclusion is composed of cuspate K-feldspar + quartz + apatite in monazite. (l) Type III gneiss 15XZ101, the rim of monazite is partially corroded by K-feldspar + apatite + thorite.

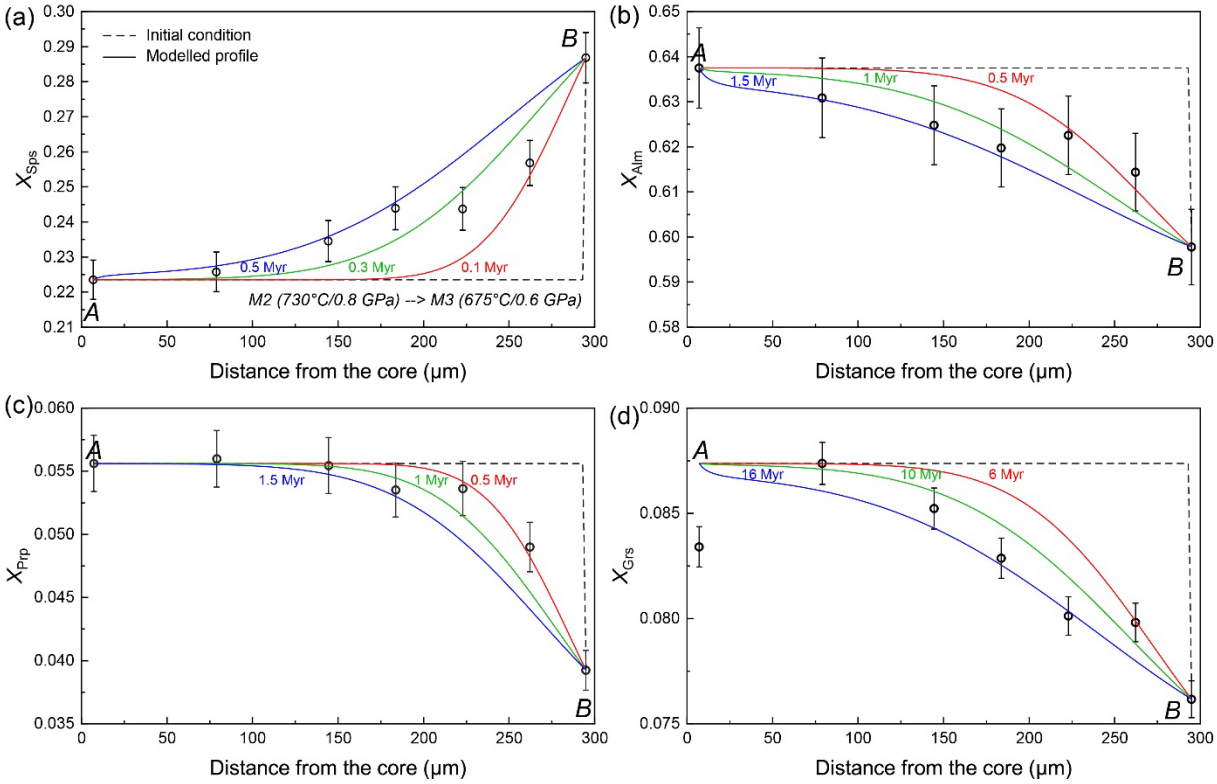


**Figure S11.** Garnet single component diffusion modeling for Type I granitic gneiss 15XZ120 from the Cona area, southern Tibet, in the eastern Himalaya. In order to quantitatively compare the diffusion rate of Mn, Fe, Mg, and Ca in garnet, we conduct spherical diffusion modeling using the newly calibrated diffusion coefficients of Chu and Ague (2015). We assume an initial homogeneous profile from core to rim (A–>B) and a contrast composition at outmost rim (B), and the boundary is fixed as the initiation. Garnet diffusion was performed under *P–T–f*$_{O2}$ conditions of 730°C to 675°C, 0.8 GPa to 0.6 GPa, and CCO oxygen fugacity from garnet core to outmost rim (A–>B). The modelled results show that the diffusion rate of Mn is the fastest, the diffusion rate of Ca is the slowest, while the diffusion rates of Fe and Mg fall in between those of Mn and Ca.

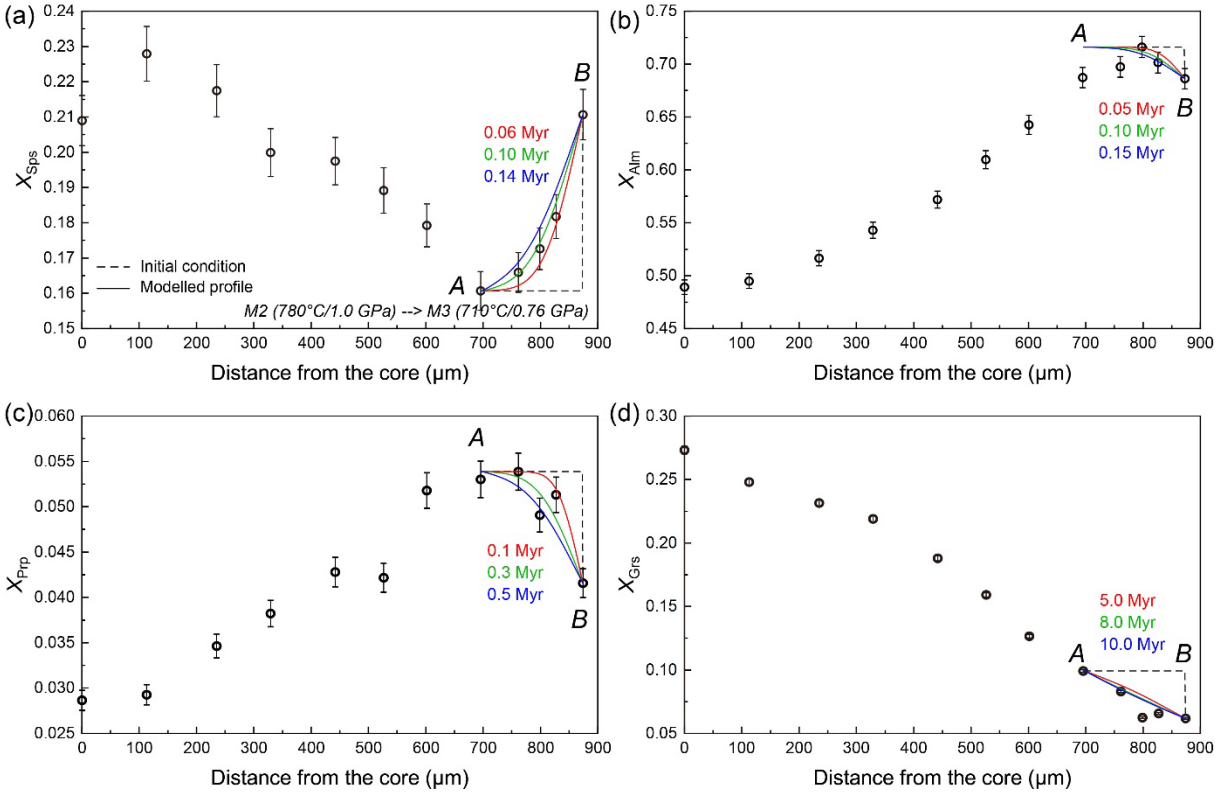


**Figure S12.** Garnet single component diffusion modeling for Type II granitic gneiss 15XZ88 from the Cona area, southern Tibet, in the eastern Himalaya. To quantitatively compare the diffusion rate of Mn, Fe, Mg, and Ca in garnet, we conduct spherical diffusion modeling using the newly calibrated diffusion coefficients of Chu and Ague (2015). We assume an initial homogeneous profile of the rim (A–>B) and a contrast composition at outmost rim (B), the boundary is fixed as the initiation. Garnet diffusion was performed and under *P–T–f*$_{O_2}$ conditions of 780°C to 710°C, 1.0 GPa to 0.76 GPa, and CCO oxygen fugacity from garnet inner rim to outmost rim (A–>B). The modelled results show that the diffusion rate of Mn is the fastest, the diffusion rate of Ca is the slowest, while the diffusion rates of Fe and Mg fall in between those of Mn and Ca.

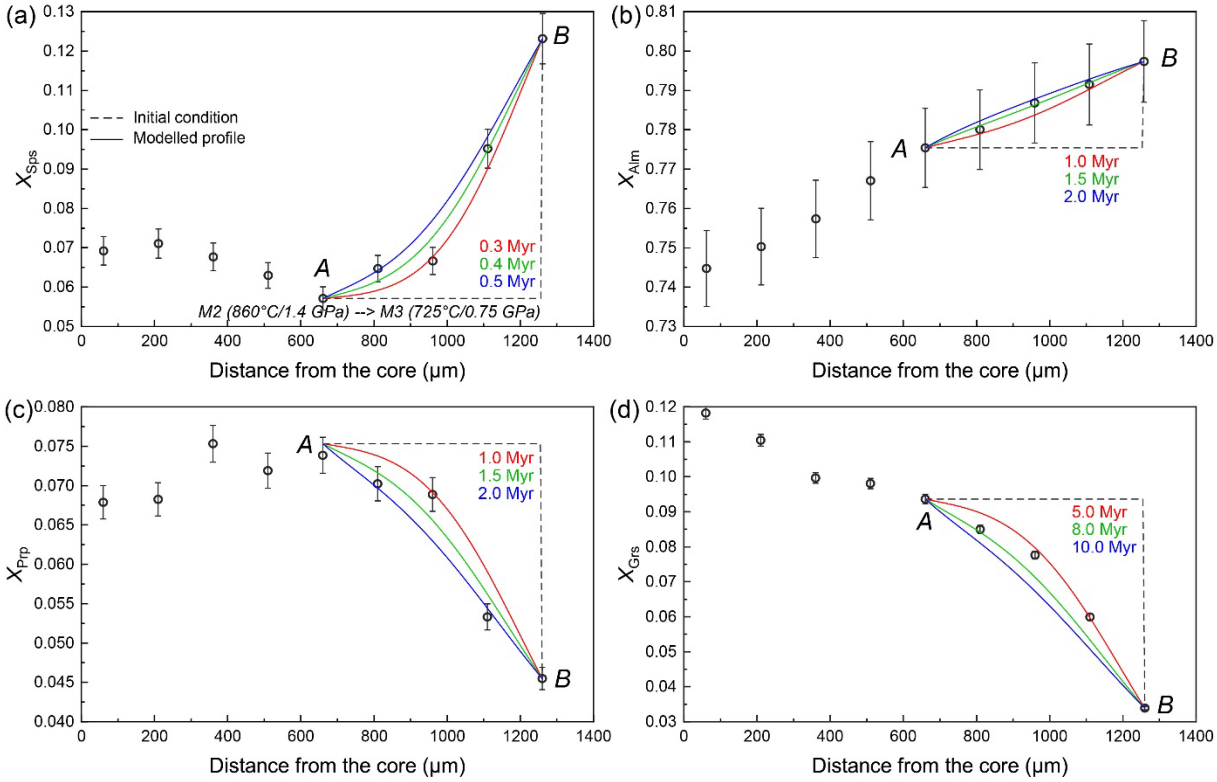


**Figure S13.** Garnet single component diffusion modeling for Type III granitic gneiss 15XZ93 from the Cona area, southern Tibet, in the eastern Himalaya. To quantitatively compare the diffusion rate of Mn, Fe, Mg, and Ca in garnet, we conduct spherical diffusion modeling using the newly calibrated diffusion coefficients of Chu and Ague (2015). We assume an initial homogeneous profile of the rim (A–>B) and a contrast composition at outmost rim (B), the boundary is fixed as the initiation. Garnet diffusion was performed and under *P–T–f*$_{O2}$ conditions of 860°C to 725°C, 1.4 GPa to 0.75 GPa, and CCO oxygen fugacity from garnet inner rim to outmost rim (A–>B). The modelled results show that the diffusion rate of Mn is the fastest, the diffusion rate of Ca is the slowest, while the diffusion rates of Fe and Mg fall in between those of Mn and Ca.

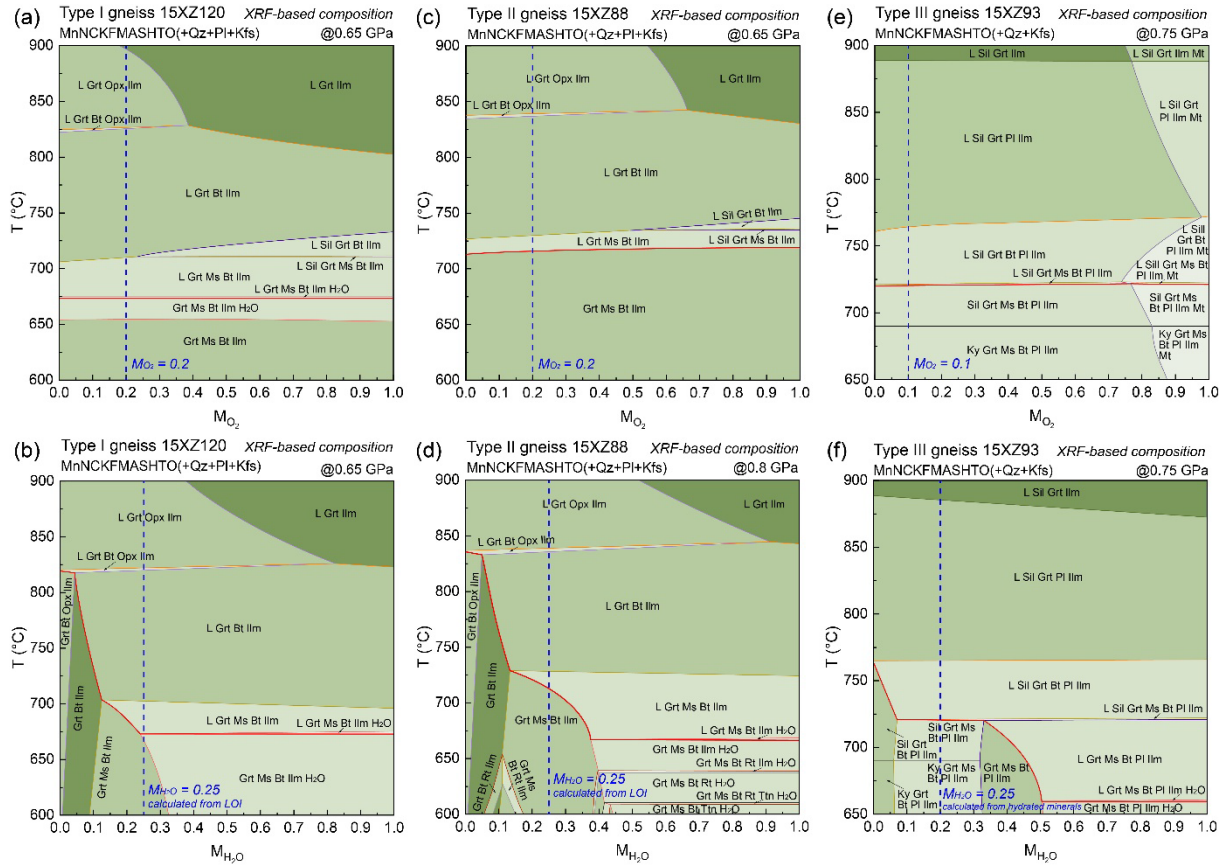


**Figure S14.** *T*–$M_{O2}$ and *T*–$M_{H2O}$ pseudosections modelled by software Perple_X 6.8.5 using XRF-based compositions for three types of granitic gneisses from the Cona area, southern Tibet, in the eastern Himalaya. (a, b) Type I granitic gneiss 15XZ120. (b, c) Type II granitic gneiss 15XZ88. (c, d) Type III granitic gneiss 15XZ93. Vertical blue dash lines in the figures denote the $O_2$($Fe_2O_3$) and $H_2O$ contents used for subsequent modeling.

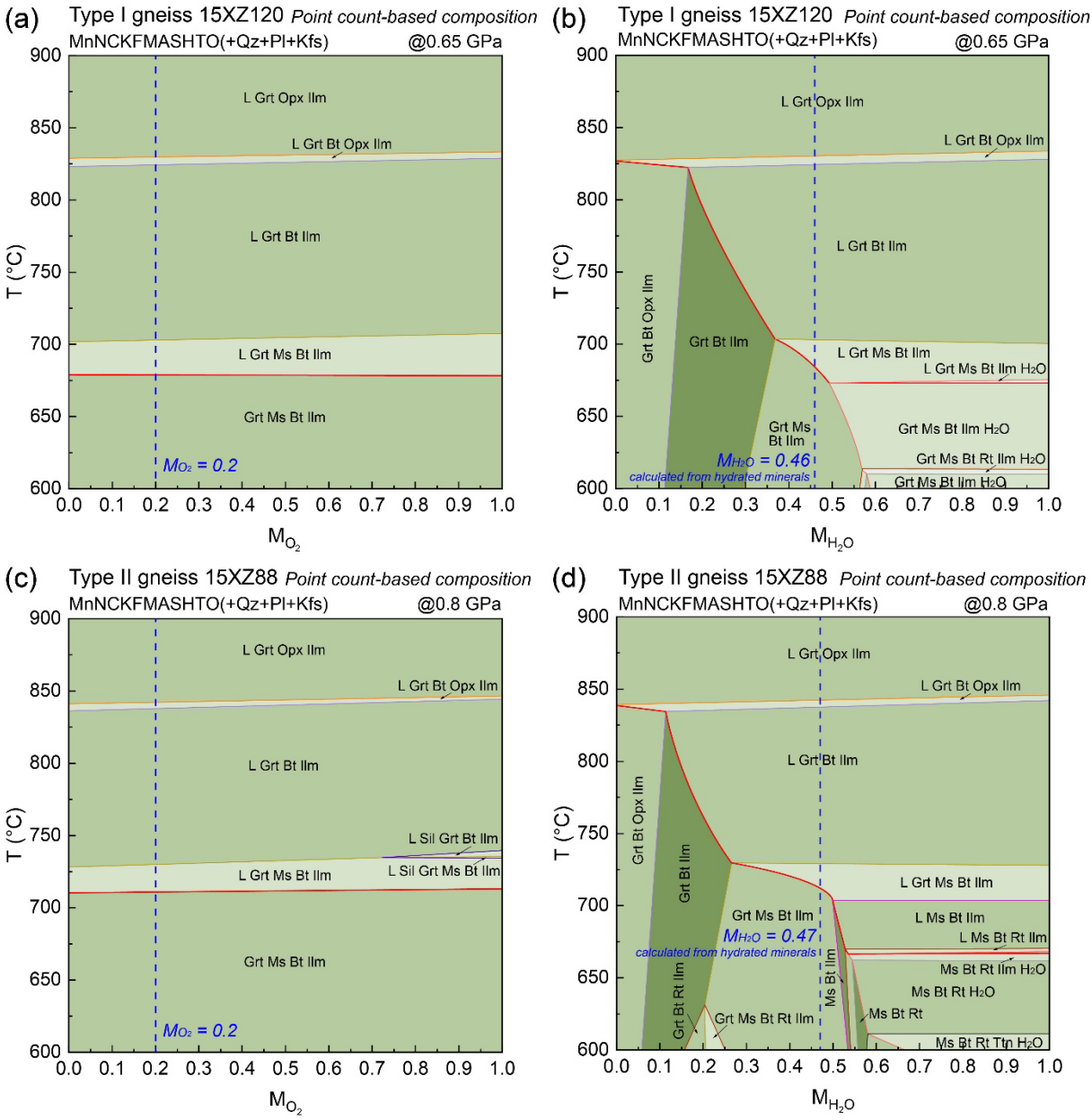


**Figure S15.** *T*–$M_{O2}$ and *T*–$M_{H2O}$ pseudosections modelled by software Perple_X 6.8.5 using point count-based compositions for Type I and II granitic gneisses from the Cona area, southern Tibet, in the eastern Himalaya. (a, b) Type I granitic gneiss 15XZ120. (c, d) Type II granitic gneiss 15XZ88. Vertical blue dash lines in the figures denote the $O_2$($Fe_2O_3$) and $H_2O$ contents used for subsequent modeling.

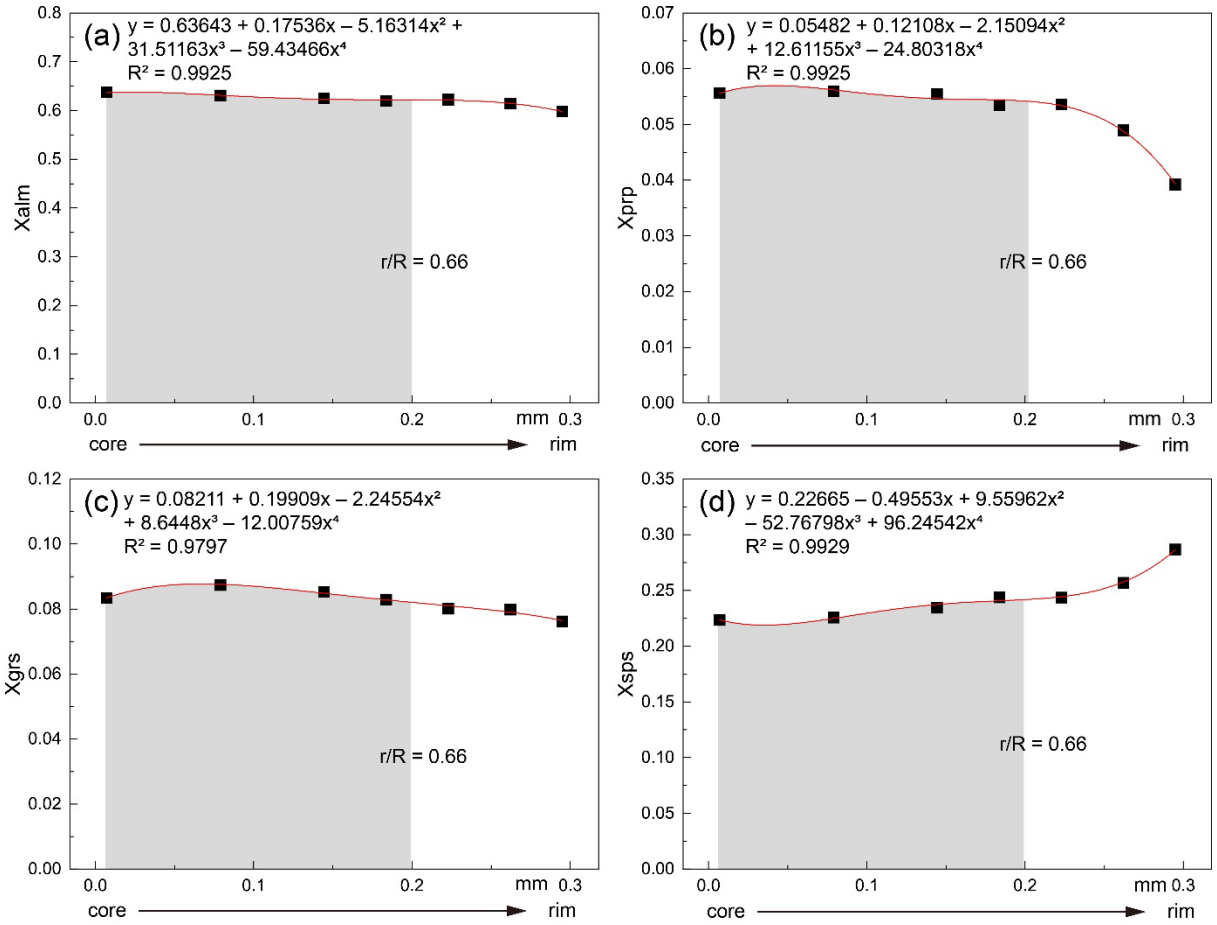


**Figure S16.** Polynomial fitting of compositional zoning as a function of x into quadrinomial for garnet from Type I gneiss 15XZ120. Inset shows the fitting functions for the almandine, pyrope, grossular, and spessartite endmembers. The grey area denotes the fractionated core, r and R represent the radius of core and bulk garnet, respectively.

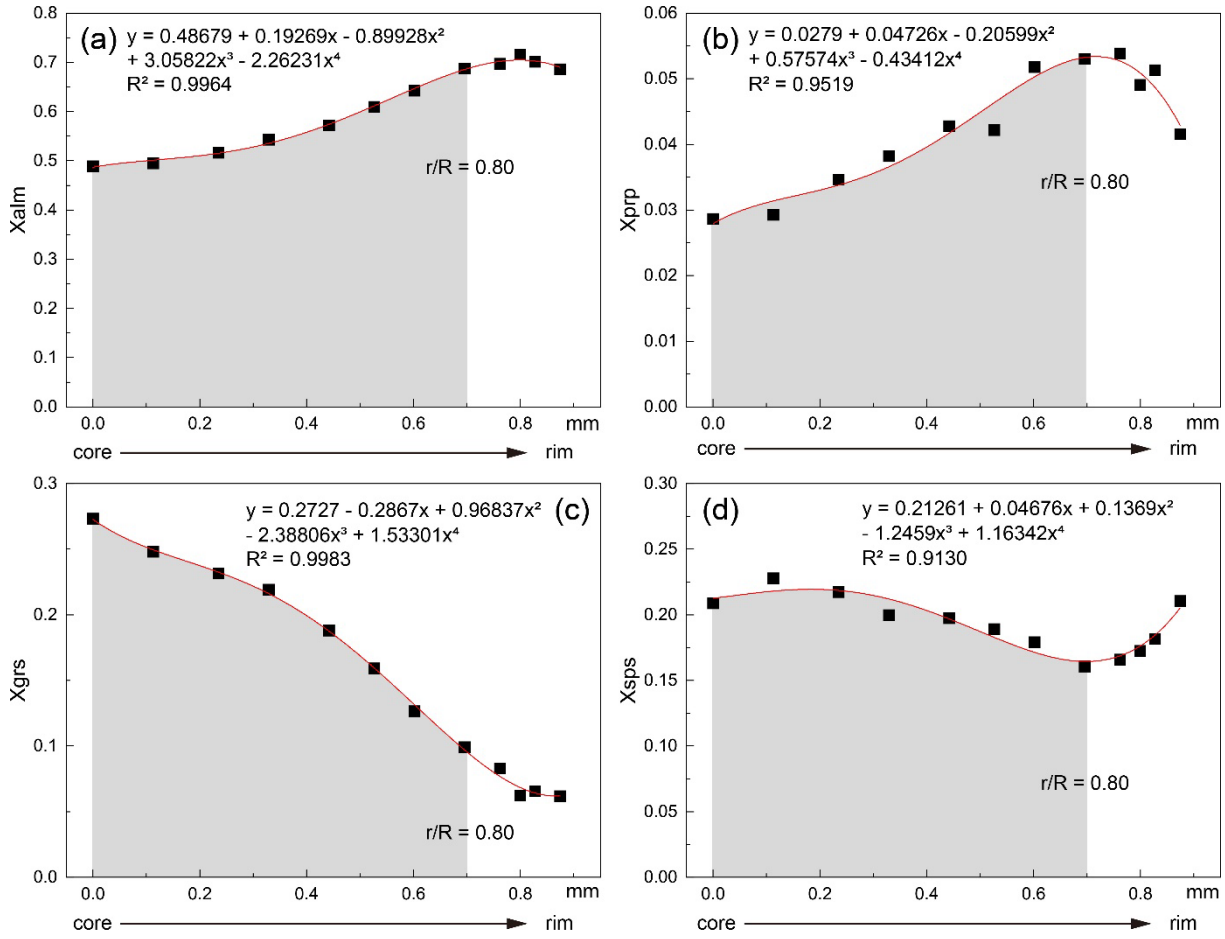


**Figure S17.** Polynomial fitting of compositional zoning as a function of x into quadrinomial for garnet from Type II gneiss 15XZ88. Inset shows the fitting functions for the almandine, pyrope, grossular, and spessartite endmembers. The grey area denotes the fractionated core, r and R represent the radius of core and bulk garnet, respectively.

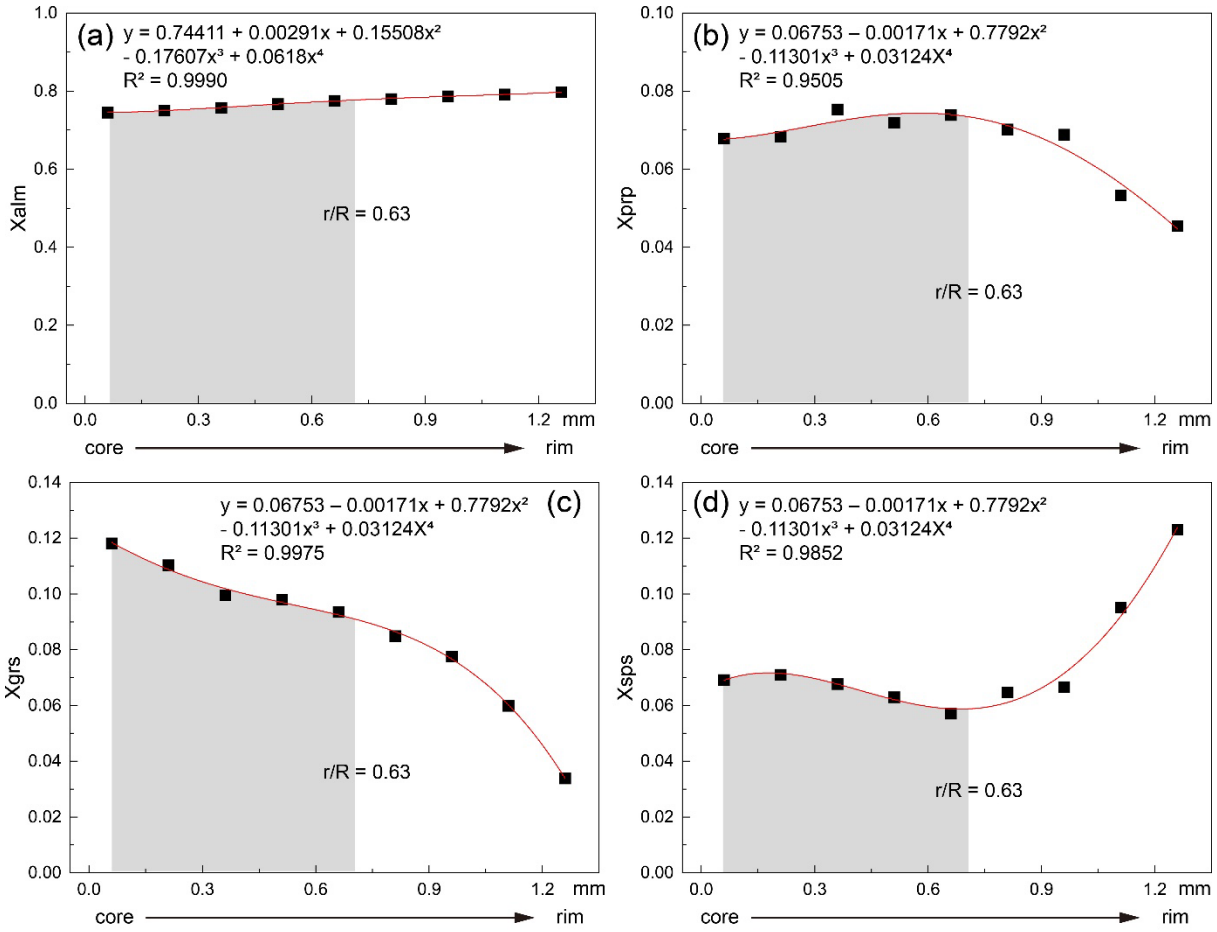


**Figure S18.** Polynomial fitting of compositional zoning as a function of x into quadrinomial for garnet from Type III gneiss 15XZ93. Inset shows the fitting functions for the almandine, pyrope, grossular, and spessartite endmembers. The grey area denotes the fractionated core, r and R represent the radius of core and bulk garnet, respectively.

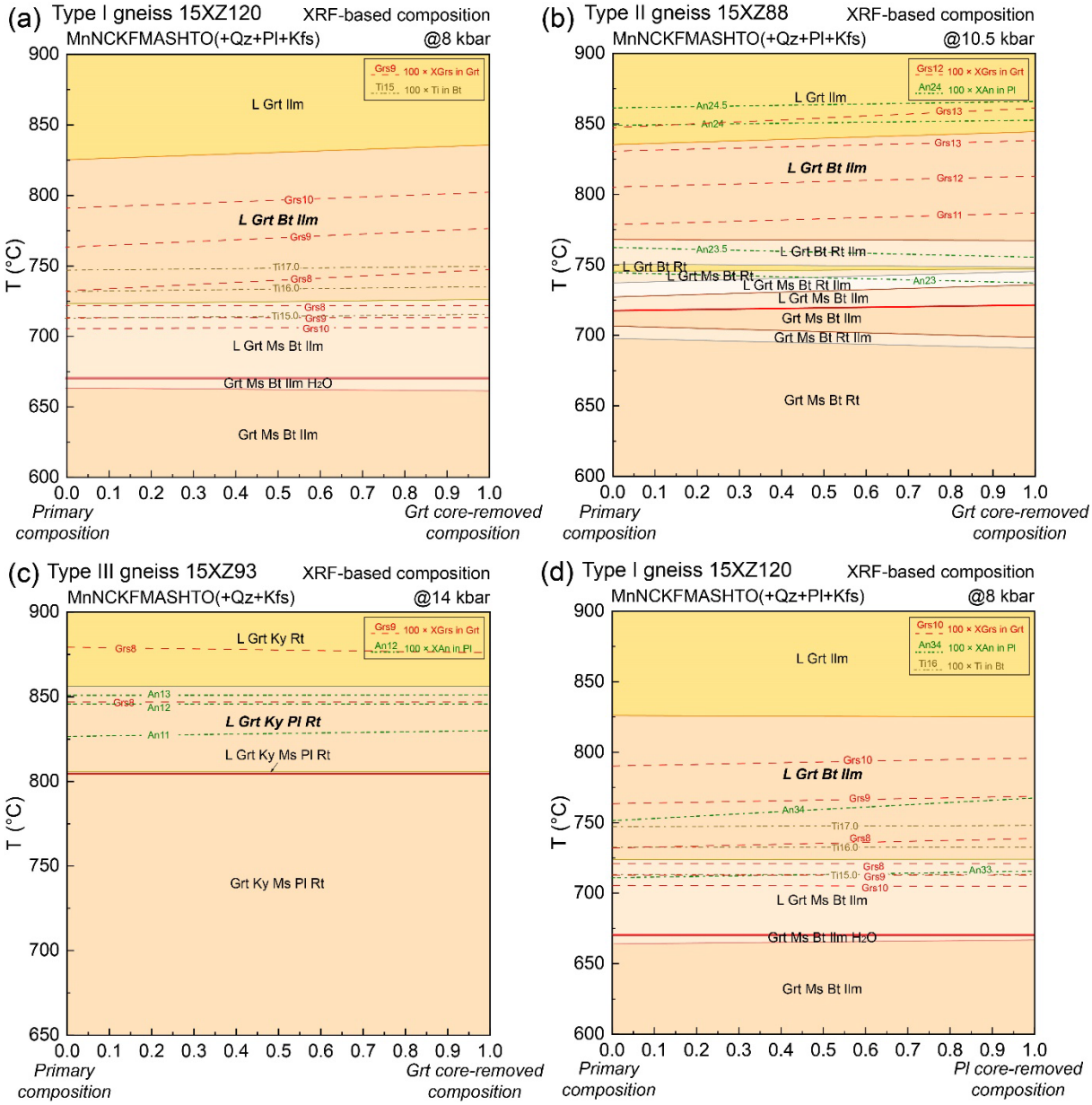


**Figure S19.** *T*–*X* pseudosections modelled by software Perple_X 6.8.5 using the primary and core-removed compositions for three types of granitic gneiss from the Cona area, southern Tibet, in the eastern Himalaya. The location where $X = 0$ represents the primary XRF-based composition, while the location where $X = 1$ represents the effective whole-rock composition from which the garnet core (a, b, c) or plagioclase core (d) is removed. The composition isopleths of $X_{Grs}$ in garnet, Ti in biotite, and $X_{An}$ in plagioclase are also shown. (a) Type I granitic gneiss 15XZ120, garnet core is removed. (b) Type II granitic gneiss 15XZ88, garnet core is removed. (c) Type III granitic gneiss 15XZ93, garnet core is removed. (d) Type I granitic gneiss 15XZ120, plagioclase core is removed. The modelled results show that whether the garnet/plagioclase core is subtracted or not has a slight effect on the topologies and mineral chemistry of the *P*–*T* pseudosection for these samples.

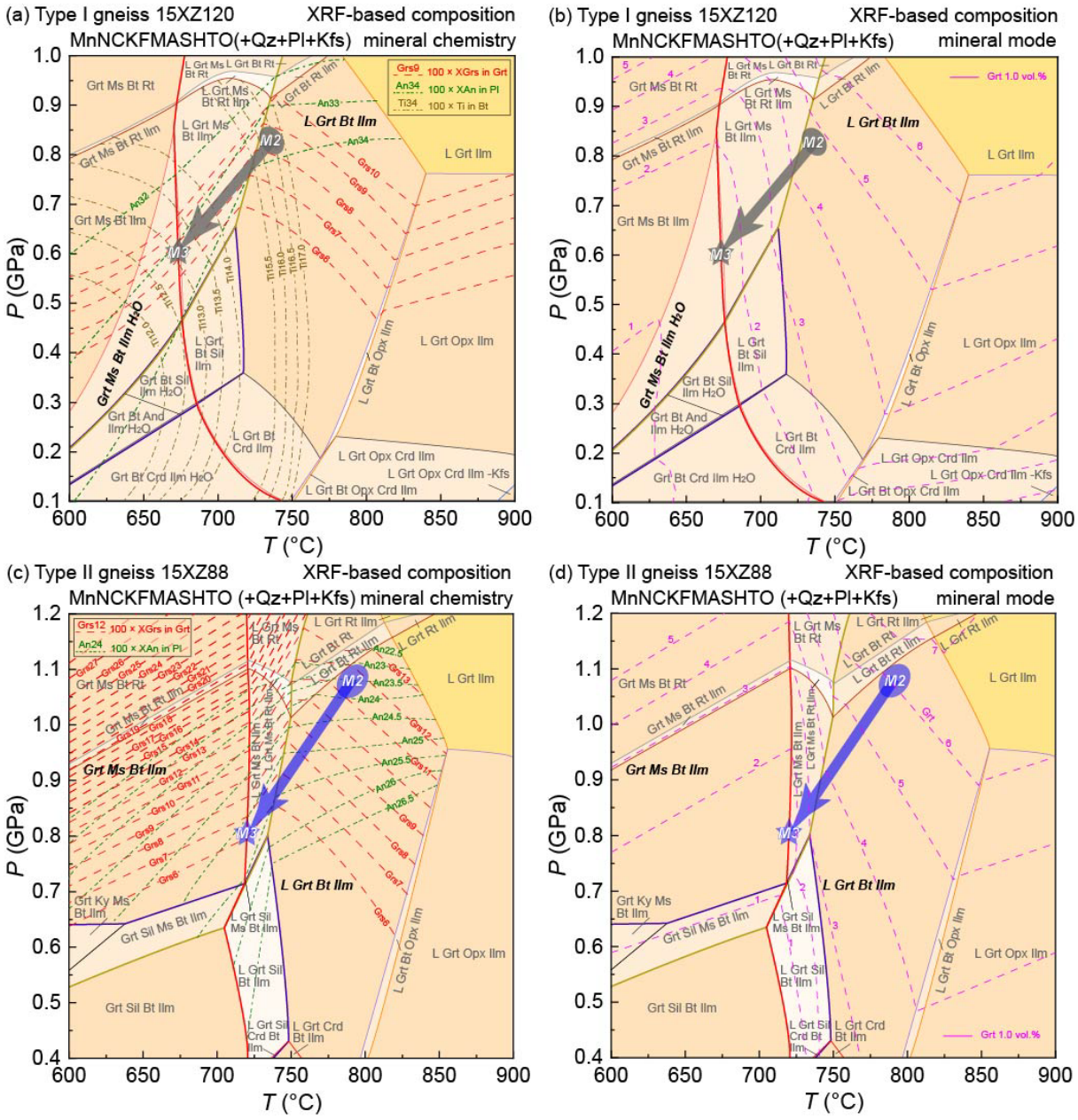


**Figure S20.** *P–T* pseudosections modelled by software Perple_X 6.8.5 using the XRF-based whole-rock compositions for Type I and II granitic gneisses from the Cona area, southern Tibet, in the eastern Himalaya. (a, b) Type I granitic gneiss 15XZ120. (c, d) Type II granitic gneiss 15XZ88.

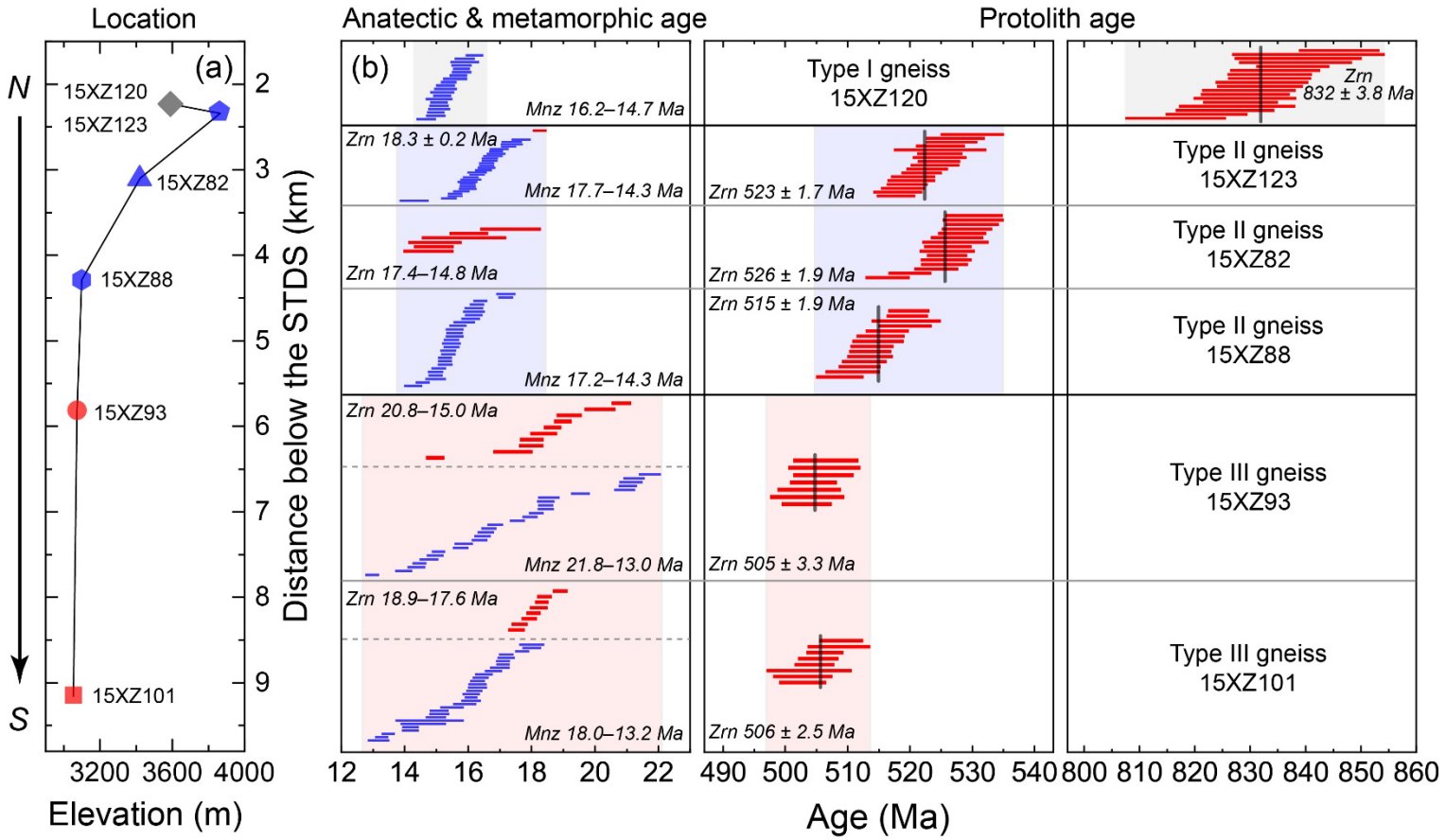


**Figure S21** (a) Zircon and monazite U–Th–Pb ages show characteristic trends against the elevations and the distances below the STDS for these dated granitic gneisses from north to south along the N-S transect. (b) Summary of zircon $^{206}Pb/^{238}U$ ages (in red color) and monazite $^{208}Pb/^{232}Th$ ages (in blue color) for three types of granitic gneisses from the Cona area, southern Tibet, in the eastern Himalaya.

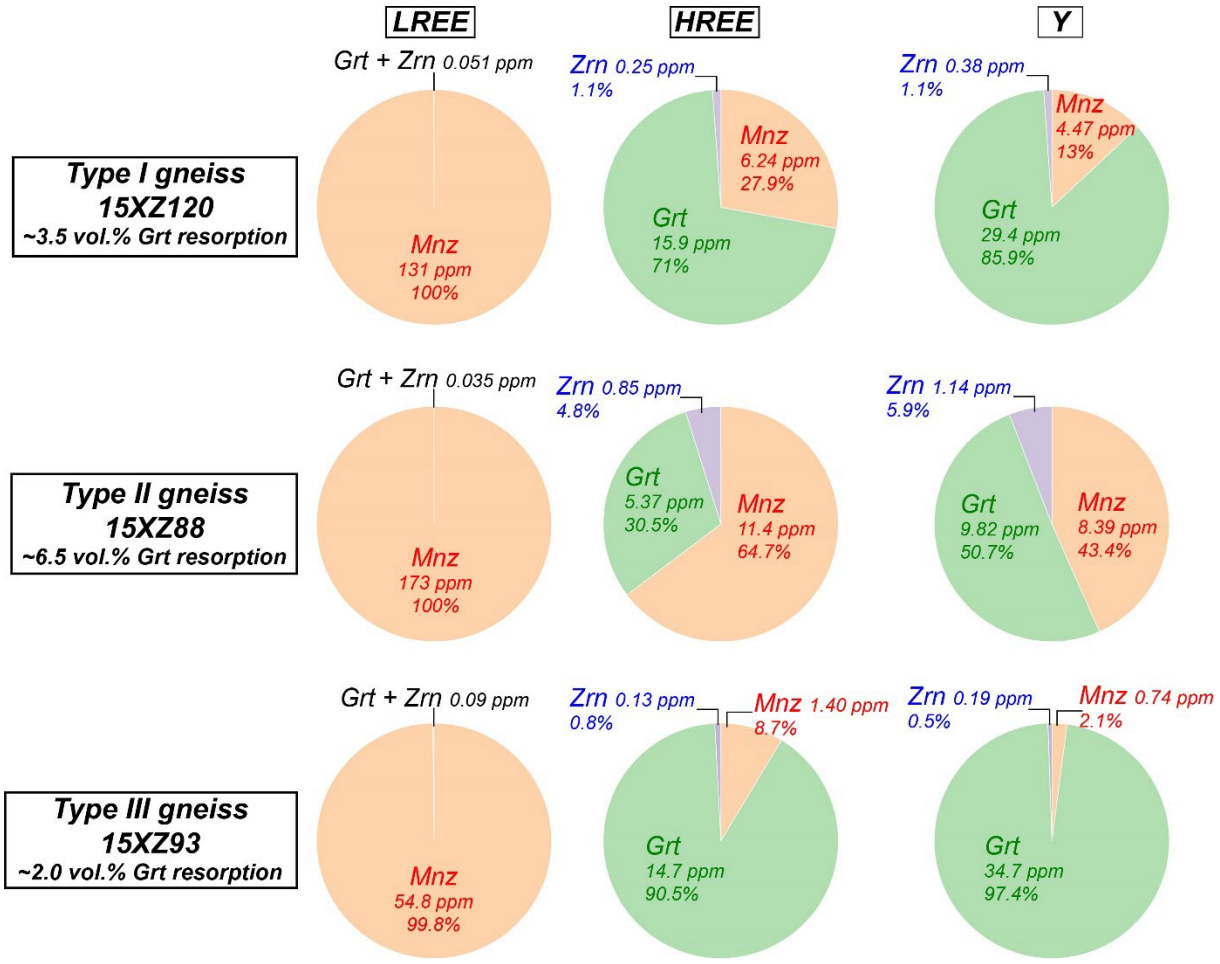


**Figure S22.** The pie chart diagrams show the light-rare earth elements (LREE), heavy-rare earth elements (HREE), and Y contents that each mineral contained according to the whole-rock trace element mass balance calculation for important REE-bearing minerals in three types of granitic gneisses from the Cona area, southern Tibet, in the eastern Himalaya.

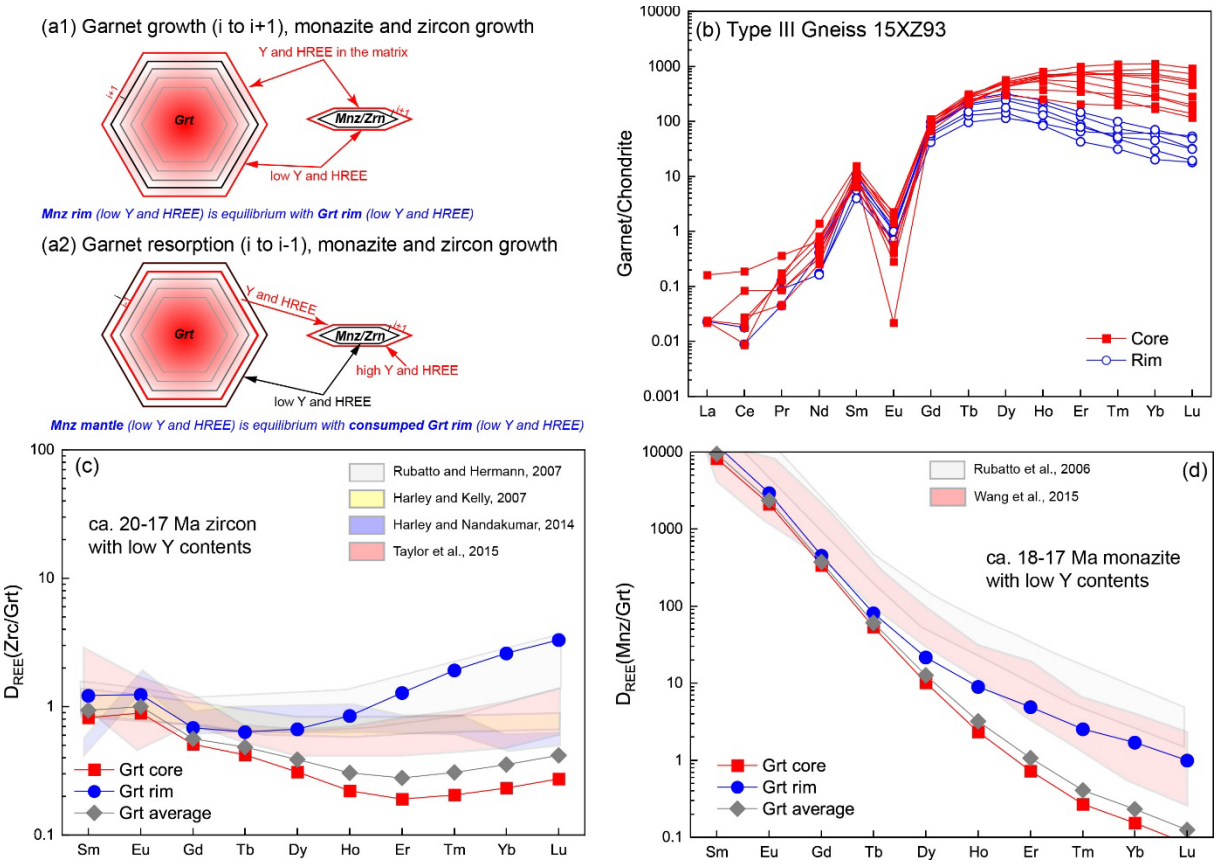


**Figure S23.** (a) A schematic diagram for trace element partition between garnet and zircon/monazite during garnet growth and resorption process. Chondrite normalized REE patterns of garnet (b) and the calculated partition coefficients of REE between zircon and garnet (c) and monazite and garnet (d) for Type III gneiss 15XZ93 from the Cona area, southern Tibet, in the eastern Himalaya.